Laser induced graphene-gold nanoparticle hybrid composite electrode towards point-of-care diagnostics

by

Kyle Duke

Submitted in Partial Fulfillment of the Requirements

for the Degree of
Master of Science

in

Chemical Engineering

YOUNGSTOWN STATE UNIVERSITY

August 2024

Laser induced graphene-gold nanoparticle hybrid composite electrode

towards point-of-care diagnostics

Kyle Duke

I hereby release this thesis to the public. I understand that this thesis will be made available from the OhioLINK ETD Center and the Maag Library Circulation Desk for public access. I also authorize the University or other individuals to make copies of this thesis as needed for scholarly research.

Signature:

_____

Kyle Duke, Student Date

Approvals:

_____

Dr. Byung-Wook Park, Thesis Advisor Date

_____

Dr. Frank Li, Committee Member Date

_____

Dr. Jonathan Caguiat, Committee Member Date

_____

Dr. Salvatore A. Sanders, Dean of Graduate Studies Date

Abstract

Wearable biosensors have become a valuable tool for their promising applications in personalized medicine. Cortisol is a biomarker for various diseases and plays a key role in metabolism, blood pressure regulation, and glucose levels. In this study, we fabricated an interdigitated laser-induced graphene (LIG) biosensor for the non-faradaic impedimetric detection of cortisol in sweat. A direct laser writing technique was used to produce the LIG. Gold nanoparticles (AuNPs) were electrochemically deposited onto the surface to enhance impedance response. A Self-Assembled Monolayer (SAM) was formed with on the AuNPs via 3-Mercaptopropionic acid (MPA) thiol chemistry. The carboxylic acid (-COOH) groups of the MPA were activated using EDC/NHS chemistry. Following activation, anti-cortisol antibodies were immobilized on the surface. Lastly, the LIG was incubated in the blocking agent bovine serum albumin (BSA) to avoid unwanted detection. Surface characterization of the LIG was performed at each step of modification by Electrochemical impedance spectroscopy (EIS) in a phosphate buffered saline (PBS) solution containing a 5 mM $Fe(CN)^{3-/4-}$ (1:1) redox couple. Further characterization of the modified LIG electrode was achieved through Fourier transform infrared (FT-IR), surfaced-enhanced Raman spectroscopy (SERS), and X-ray diffraction (XRD). The detection experiment using EIS was conducted in increasing concentrations of cortisol (0.1 pM-100 nM) in PBS. The Z_{Mod} decreased logarithmically (R^2=0.97) with a 0.0085 nM limit of detection. Reproducibility was examined by percent change of Z_{Mod} at 100 nM and a 5.93%RSD (n=5) was observed. Additional analysis of sensor specificity and interference studies showed no substantial effect on detection. This research

establishes the feasibility of using the gold nanoparticle decorated LIG electrode for flexible, wearable cortisol sensing devices, which would pave the way towards an end-user easy-to-handle biosensors as point-of-care diagnostics.

Table of Contents

Acknowledgment

I would like to take this opportunity to thank those that have supported and guided me throughout my graduate studies. Firstly, I extend my upmost respect and gratitude to my advisor Dr. Byung-Wook Park. He has been a constant source of encouragement and motivation since day one. Under his guidance and support I have learned valuable skills that will help me succeed in the engineering field.

I would also like to thank Dr. Frank Li, Dr. Jonathan Caguiat, and Dr. Pedro Cortes for their roles for advising and teaching me various subjects throughout my graduate studies, and Mr. Ray Hoff for helping me access and operate characterization instruments necessary to complete my thesis. I would also like to thank my lab mates, Jose Gonzalez Garcia, Kyle Preusser, Victoria Messuri, and Prakriti Dhungana, for their motivation and support. As well as my friend DJ for helping me out during stressful times in my studies.

Lastly, I would like to thank my mom, dad, and sister for their invaluable support throughout my graduate and undergraduate studies. Without their encouragement and support, this would be impossible.

List of Figures

List of Tables

List of Abbreviations

AuNPs: Gold Nanoparticles

LIG: Laser Induced Graphene

HPA: HypothalamusPpituitary-Adrenal

SPR: Surface Plasma Resonance

ELISA: Enzyme-Linked Immunosorbent Assay

EIS: Electrochemical Impedance Spectroscopy

CV: Cyclic Voltammetry

QCM: Quartz Crystal Microbalance

PI: Polyimide

RE: Reference Electrode

WE: Working Electrode

CE: Counter Electrode

IDE: Interdigitated Electrode

SEM: Scanning Electron Microscopy

EDX: Energy Dispersive X-ray Spectroscopy

SCE: Saturated Calomel Electrode

AC: Alternating Current

DC: Direct Current

POC: Point of Care

EDL: Electrical Double layer

MB: Magnetic beads

AChE: Acetylcholinesterase

DPV: Differential Pulse voltammetry

LOD: Limit of Detection

MOFs: Metal Organic Frameworks

NFC: Near-Field Communication

SWV: Squarewave Voltammetry

3-MPA: 3-Mercaptopropionic acid

EDC: 1-Ethyl-3-(3-dimethylaminopropyl)carbodiimide

NHS: N-Hydroxysulfosuccinimide sodium salt

MES: 2-(N-morpholino) ethanesulfonic acid

PBS: Phosphate-buffered Saline

DPI: Dots Per Inch

BSA: Bovine Serum Albumin

Ab: Antibody

XRD: X-ray Diffraction

MIP: Molecularly Imprinted

PDMS: Polydimethylsiloxane

HRP: Horseradish Peroxidase

HQ: Hydroquinone

1. Introduction

1.1. Background

1.1.1. Cortisol

Cortisol is a steroid hormone that is synthesized in the zona fasciculata of the adrenal cortex and considered as a crucial biomarker regulated by the stress-responsive hypothalamus-pituitary-adrenal (HPA) axis response. In regulates various physiological mechanisms involved in several metabolic, anti-inflammatory, immune system, and anti-stress pathways [1]. Abnormal levels of cortisol inhibit weight loss, low blood pressure, fatigue, muscle weakness, inflammation, high blood sugar, obesity, and fragile skin [2]. Continuous monitoring of cortisol is important to understand the how cortisol impacts various health conditions such as chronic stress or mental health issues [3]. A cortisol test measures the level of cortisol in saliva, blood, urine, sweat and interstitial fluids in clinical laboratories. Clinical studies have demonstrated a correlation between free cortisol levels in saliva and blood. In particular, sweat cortisol levels were found to be correlated with salivary cortisol concentrations. The cortisol concentration in sweat was found to be from 1 to 141.7 ng/ml [4, 5]. Thus, the precise measurement of cortisol in sweat is known as a challenging process, as it requires high sensitivity compared to other forms of cortisol. Conventional techniques such as enzyme-linked immunosorbent assay (ELISA) [6], chromatography, surface plasmon resonance (SPR) [7], and quartz crystal microbalance (QCM) [8], have been widely used in clinical diagnosis and biochemical research laboratories. However, the operation process on these methods is complex and

incompatible with continuous and remote monitoring, and requires multiple procedures for purification of samples [3].

1.1.2. Laser induced graphene

Graphene is an allotrope of carbon consisting of a single one atom layer of carbon atoms arranged in a hexagonal pattern [9]. The chemical properties and planar structure of graphene provide various advantages over other materials, particularly for sensor applications. The large surface area of graphene allows for heightened sensitivity to chemical and physical changes in the local environment [10]. Another advantage of graphene is its cheap production cost compared to other commonly used materials [11].

First reported in 2014, laser induced graphene (LIG) is a porous material prepared by direct laser writing a polyimide film (PI) with a CO_2 laser at ambient conditions. The formation of LIG involves the conversion of the substrates sp^3 hybridized carbon atoms to graphene's sp^2 hybridization. Specifically, direct laser writing breaks the weak carbon nitrogen bonds of the PI film, forming graphene and various other unstable compounds [12].

The resulting LIG exhibits a high surface area, great conductivity, thermal stability, and flexibility [13]. LIG has several advantages over conventional graphene such as patternability, tunable compositions, and controllable morphologies [14].
Due to its desirable properties, LIG has been utilized in a wide range of applications such as electronics, energy storage, medical fields, and most notability sensors [15, 16].

1.1.3. Electrochemical biosensors

A biosensor is an analytical device that incorporates a biological sensing element (enzyme, antibody, DNA, cell) with a physiochemical transducer that can detect and convert biological activity into a measurable signal [17]. Electrochemical biosensors are widely used due to their specificity, portability, low cost, and point of care capabilities [18]. They can be broken down into four subcategories : (1) Potentiometric, (2) Amperometric, (3) Conductometric, and (4) Impedimetric [19].

The basic structure of an electrochemical biosensor is depicted in **Figure 1.1.** [20]. It is composed of a biological sensing element (enzyme, protein, DNA, antibody, etc.) that interacts with a specific analyte, producing an electrical signal which can then be processed and related to the concentration of the analyte.

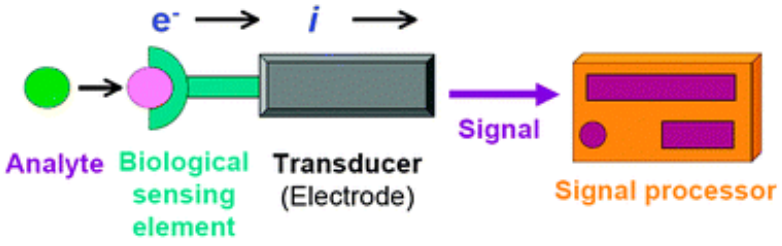

Figure 1.1. Schematic of a electrochemical biosensor [20].

They are incorporated into a 2-electrode or 3-electrode electrochemical cell. The 3-electrode system shown in **Figure 1.2.** [21], consists of a working electrode (WE), reference electrode (RE), and a counter electrode (CE). The biosensor serves as the WE and is where the desired reaction with the analyte occurs. The RE, typically an Ag/AgCl or saturated calomel electrode (SCE) provides a constant and defined potential across the

cell. While the CE, most commonly platinum, completes the circuit and allows for current to flow through.

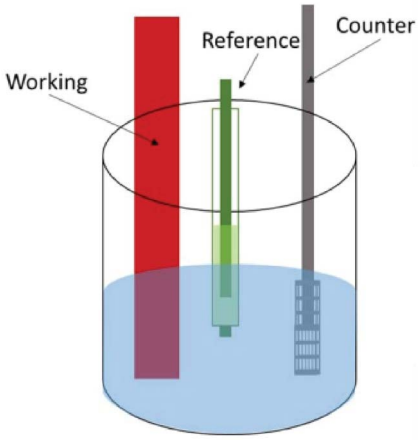

Figure 1.2. Schematic of a conventional 3-electrode electrochemical cell [21].

Less commonly used is the 2-electrode system, which consists of a working electrode and one electrode that serves as both the counter and reference electrode. However, when applicable, they are preferred over 3-electrode systems due to their long term stability, and cost reduction [20].

1.1.4. Interdigitated electrode

Interdigitated electrodes (IDEs), as depicted in **Figure 1.3.**, have a 2-electrode configuration with two alternating comb-like structures [22]. The small gap between the combs increases sensitivity, response times, and signal to noise ratios [23]. Additionally, adjusting the gap width and other geometric properties directly influences its electrical properties (i.e. capacitance and impedance) [24]. Meaning, IDEs can be essentially

tailored to suit the desired application. Furthermore, it has many advantages over other electrode configurations such as increased surface area, miniaturization capabilities, and low cost due to the removal of the reference electrode [25, 26].

Perhaps unsurprisingly, IDEs have been implemented in a diverse array of biosensors since it was first reported in the 1990s. In recent years, researchers have focused on the use of IDEs in non-faradaic and label-free biosensors.

Figure 1.3. Schematic of a laser induced graphene interdigitated electrode (IDE).

1.1.5. Non-faradaic and faradaic EIS

Electrochemical impedance spectroscopy (EIS) is a technique commonly used to analyze bio-recognition events that take place on the electrode surface [27]. In EIS, an alternating current (AC) is applied to create a small perturbation over a wide range of frequencies, and the current in response to the perturbation is recorded. The impedance (opposition to current flow) can then be calculated at each frequency, providing an insight into the bio-recognition events taking place. Typically, data is represented in the form of a Bode plot and a Nyquist plot. In a bode plot, the log of the magnitude of impedance ($\log|Z|$) and the phase angle (θ) are plotted against the log of the frequency

(log(*f*)) to see the effect frequency has on the impedance of a system. Whereas a Nyquist plot, plots the imaginary impedance (Z_j) versus the real impedance (Z_r).

Equivalent circuit models are commonly used to represent the impedance of the system in terms of electrical components (resistors, inductance, and capacitors) providing information on the electrochemical properties taking place in the cell. The equivalent circuit model is chosen based on the exhibited characteristics. The most commonly used models are variations of Randles equivalent circuit (**Figure 1.4.**) [28].

Faradaic-EIS is EIS with the use of a redox couple (i.e. ferri/ferrocyanide) where detection relies on impedance changes due to the redox reactions taking place. On the other hand, non-faradaic-EIS has no redox couple, and direct current (DC) based impedance occurs [27]. When it comes to impedance-based biosensors, there are key advantages and disadvantages.

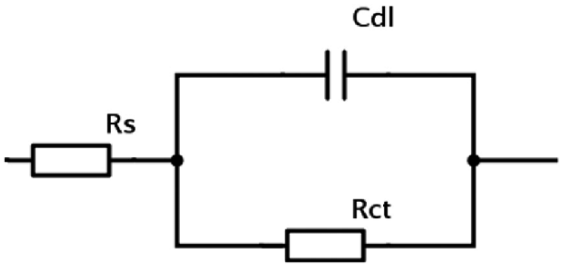

Figure 1.4. Schematic representation of modified Randles equivalent circuit [28].

1.1.6. Non-faradaic impedimetric immunosensors

Impedimetric immunosensors are biosensors that measure the change in impedance caused by the interaction between the immobilized antibody (biorecognition element) and antigen (analyte) [29]. Among the different forms of detecting this

interaction, impedance is particularly attractive due to the low cost of electrode mass production, cost effective instrumentation, and the ability to be miniaturized [30]. Furthermore, under non-faradaic conditions, there is no redox mediator and the reference electrode is unnecessary, and is therefore favored for real-time measurements and consequently point of care (POC) applications [31].

In non-faradaic impedimetric immunosensors, the change in impedance is caused by the antibody-antigen complex formation in the electrical double layer (EDL) at the electrode solution interface [32]. In the frequency range of 5-1000 Hz, the capacitance of the double layer (C_{dl}) becomes more prominent in the impedance response, and is inversely proportional to the magnitude of the impedance [33]. Sensor calibration is achieved by observing the percent change in $|Z|$ at a specific frequency within this region. Consequently, the frequency range of EIS can be reduced to single frequency EIS for detection.

1.1.7. Electrodeposited AuNP-based biosensors

Electrodeposition is a process that utilizes a redox reaction to form a uniform coating on an electrode by applying current through an electrochemical cell [34]. It is achieved primarily through galvanostatic, voltammetric, and potentiometric techniques. The morphology of the nanostructures can be adjusted by manipulating factors such as the electrolyte composition, applied potential, current, and temperature [35]. It has seen widespread use by researchers in the biosensor field for its cost-effectiveness, time, and energy-saving nature.

Gold nanoparticles (AuNPs) are the most popular choice in biosensor applications due to its ability to retain the biological activity of immobilized biomolecules and its facilitation of electron transfer between the immobilized proteins and electrode surface [36].

Antibodies can be immobilized on AuNPs through physical adsorption, covalent bonding, non-covalent bonding, and various other physical interactions [37]. Physical adsorption and non-covalent bonding are less commonly used because they require high antibody concentrations, antibodies are randomly oriented, and overall less stable then covalent-bonds [38]. EDC/NHS chemistry is a well-known two step covalent immobilization technique that allows for oriented and densely packed immobilization of biomolecules. In addition to the immobilization of biomolecules, they are regularly used in optical-based sensors for its ability to enhance changes in the refractive index and improve electron transfer [39].

1.2. Objectives

The purpose of this study is to first fabricate a LIG based cortisol biosensor and characterize its properties physical, chemical, and electrochemical properties. The developed biosensor will then be used to perform a detection of cortisol. The objective of this study is to evaluate the performance of the fabricated biosensor in terms of sensitivity, reproducibility, specificity, repeatability, and synthetic sweat-based detection experiments. The project was carried out in the following manner:

- Optimizing LIG production by performing a power dose assay.
- Fabricating the LIG IDE and modifying the electrode surface for development of the cortisol biosensor.
- Characterizing the material properties of the biosensor through EIS, CV, XRD, SEM, EDX, Raman spectroscopy, and FT-IR analysis.
- Performing cortisol detection over biological range found in sweat.
- Evaluating the performance of the cortisol biosensor in terms of reproducibility, specificity, repeatability, and synthetic sweat-based detection.
- Demonstrating the detection of cortisol using a hydrogel-based pad design.

1.3. Organization

This thesis will be broken down into the following chapters:

- Chapter 1 provides an introduction to concepts related to the project, the objective, and scope of work.
- Chapter 2 contains a literature review of the previous studies similar to this project.
- Chapter 3 discusses the materials and methodology of the project.

- Chapter 4 presents and discusses the results of the project.
- Chapter 5 provides concluding remarks and recommendations.

1.4. Scope of work

The overarching goal of this project is to fabricate and optimize a Laser induced graphene (LIG) based biosensor for the detection of cortisol levels in sweat. The surface properties were then characterized through XRD, Raman spectroscopy, FT-IR, and SEM-EDX. Further electrochemical characterization was performed in EIS. Furthermore, reproducibility and repeatability measurements were conducted to verify surface modifications. Specificity experiments and detection in synthetic sweat were conducted to evaluate the sensors affinity to cortisol and the effect of interferents on performance.

2. Literature review

2.1. Sweat based cortisol biosensors

Sweat based biosensors have garnered considerable attention in recent years for their point of care (POC) applications. Cortisol analysis through sweat offers a non-invasive and convenient alternative to blood and urine analysis, both of which require multiple samples due to levels changing throughout the day. Sweat-based detection is of particular interest, since it can be placed into a wearable platform, allowing for real time monitoring and POC applications.

EIS is a commonly used approach for sweat based cortisol detection. Kinnamon et al. employed vertically aligned metal electrodes with cortisol antibodies immobilized on MoS2 nanosheets. The sensor exhibited a wide linear range and an LOD of 1 ng/mL. Additionally, the sensor showed stability and flexibility, with less than 3% change in impedance over 60 bending cycles [40]. Another wearable device was reported in a 2020 article by Lee et al. The wearable platform (**Figure 2.1.**) used a microfluidic device for precise collection and delivery of sweat to the sensing element. After sufficient incubation of sweat a button containing a redox mediator is pressed, washing away the sweat into a designated disposal area, and introducing the mediator in the sensing area. Calibration was achieved by fitting the EIS data to obtain the R_{ct} over 1pg/mL to 1 µg/mL of cortisol. The electron transfer resistance increased linearly over the entire range with a sensitivity comparable to previous works [41]. Similarly a $Ti_3C_2T_x$ MXene-loaded laser induced graphene sensor was integrated with a microfluidic device for on-body measurement of cortisol through change in R_{ct} [42].

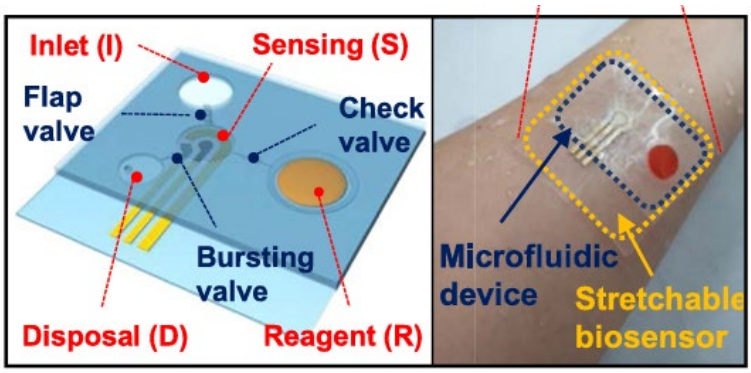

Figure 2.1. Schematic of the wearable cortisol sensor (left) and a picture of the sensor attached to the forearm (right) [41].

Amperometry has also been utilized for sweat-based cortisol detection. Fiore et al. reported a wearable paper-based microfluidic biosensor (**Figure 2.2.**) with Near-field communication (NFC). The sensor utilized magnetic beads (MB) functionalized with monoclonal antibodies for cortisol recognition, and the acetylcholinesterase (AChE) labeled cortisol for signal generation. Current was generated through the mechanism portrayed in **Figure 2.2.**, where Competition occurs between the cortisol in sweat and labeled cortisol for boding to the antibody on the magnetic bead. The amount of cortisol is quantified based on the current generated by the enzymatic reaction of AChE, which is inversely proportional to cortisol concentration. On-body experiments during exercise exhibited a change in current, indicating the successful detection of cortisol [43]. Laochai et al. reported a faradaic based potentiometric sensor with a MXene-coated conductive thread working electrode. AuNPs were electrochemically deposited on the conductive thread using chronoamperometry at −0.6 V for 120 s, and then antibodies were immobilized on the AuNPs via EDC/NHS chemistry. CV characterization showed coating the fibers in MXene increased the active surface area for AuNP formation

allowing for higher levels of antibody immobilization The fabricated sensor showed stability over a six-week period and a reproducibility of 3.46 %RSD [44].

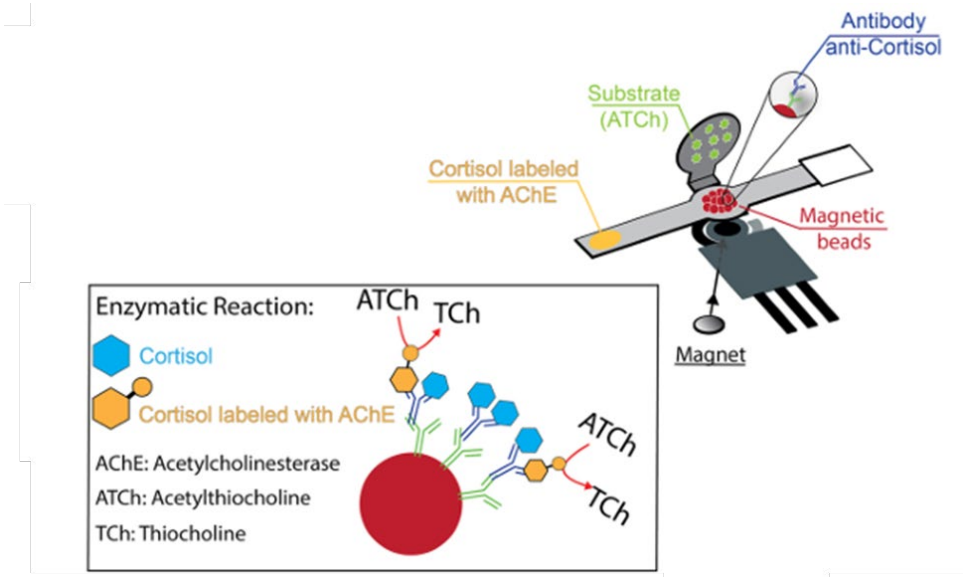

Figure 2.2. Schematic representation of the microfluidic sensor with its corresponding reaction mechanism [43].

A voltammetric reagent-less aptamer sensor was presented by Karuppaiah et al. A cortisol aptamer was conjugated with methylene blue to function as a charge carrier. The aptamers were first modified with amine groups for methylene blue conjugation and thiol functional groups to bond the aptamer to the gold surface through Au-S bonds. When cortisol bonded to the aptamer, a change in conformation charge distribution caused a decrease in the current generated. Detection was performed using Differential pulse voltammetry (DPV) and achieved a linear response between 0.05 and 100 ng/mL with a limit of detection (LOD) of 0.05 ng/mL. Additionally, specificity studies showed the

sensor exhibited little response in the presence of similarly structured molecules (**Figure 2.3.**) [45].

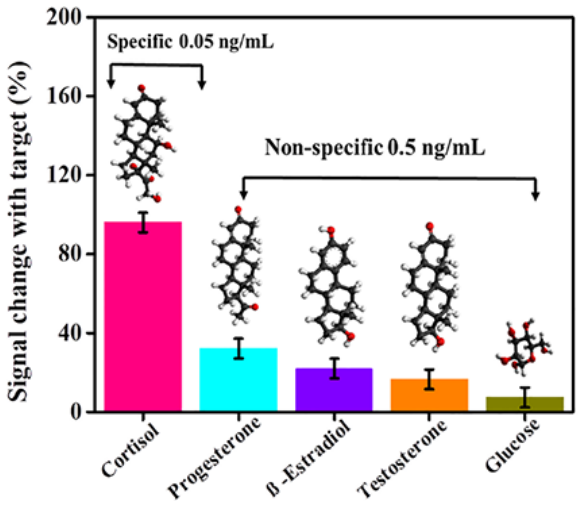

Figure 2.3. Specificity of the E-AB sensor in the presence of cortisol at 0.05 ng/mL and structurally similar molecules at a 0.5 ng/mL [45].

Similarly, Mugo et al. reported a molecularly imprinted (MIP) voltammetric sensor for cortisol detection. It was fabricated using layer-by-layer assembly, incorporating polydimethylsiloxane (PDMS) with carbon nanotubes-cellulose nanocrystals (CNC/CNT) as conductive nanofilms. Detection was conducted by Cyclic voltammetry achieving an LOD of 2 ng/mL over a dynamic range of 10-66 ng/mL [45]. In another study, cortisol antibodies were immobilized in a metal organic frameworks (MOFs) for DPV detection of cortisol. To evaluate the efficacy an on body continuous monitoring of cortisol was conducted (**Figure 2.4.**), and the sensor showed the cortisol levels constantly decreased throughout the day which correlates to the circadian rhythm of cortisol [46].

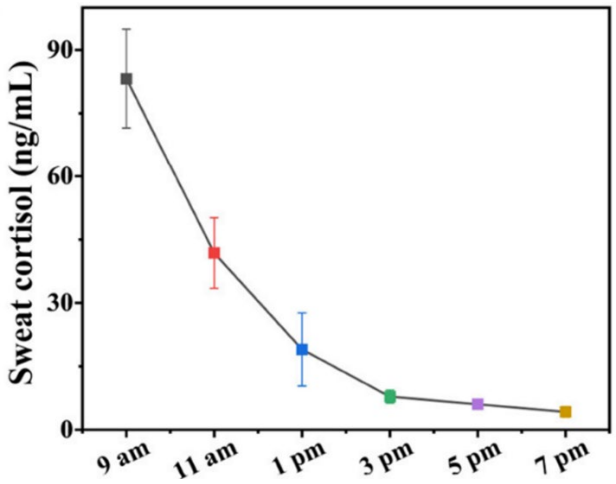

Figure 2.4. Continuous sweat cortisol monitoring throughout the day using a wearable cortisol biosensor [46].

To conclude, various sweat-based biosensors have been developed for the detection of cortisol. Voltammetric, impedimetric, and potentiometric based sensors have been reported. These sensors typically immobilize anti-cortisol antibody on the surface of the sensor for detection. Wearable platforms have been fabricated with the implementation of NFC or Bluetooth communication for real-time monitoring. Overall, recent developments in sweat-based cortisol sensors have shown potential for widespread use in POC applications.

Table 1.1. Summary of sweat-based cortisol biosensors.

Setup	Method	Buffer media	Linear range	Limit of Detection	Reference
3-electrode non-faradaic	CA	Artificial sweat	10-140 ng/mL	3 ng/mL	[43]
3-electrode faradaic	EIS	PBS	10 pM-100 nM	0.0287 ng/mL	[47]
2-electrode faradaic	EIS	PBS	1 pg/ml-10 ng	0.001 ng/mL	[41]
3-electrode non-faradaic	DPV	PBS	0.05-100 ng/mL	0.05 ng/mL	[45]
2-electrode non-faradaic	EIS	PBS	-	1 ng/mL	[40]
2-electrode non-faradaic	CV	PBS	10-66 ng/mL	2 ng/mL	[48]
3-electrode faradaic	EIS	Artificial sweat	1 pg/mL-1 µg/mL	1 pg/mL	[41]
3-electrode faradaic	CA	PBS	5-40 ng/mL & 40-180 ng/mL	0.54 ng/mL	[44]
3-electrode non-faradaic	DPV	PBS	1 pg/mL-1µg/mL	0.26pg/mL	[46]

2.2. LIG-based Electrochemical immunosensors.

In recent years, laser induced graphene (LIG) based biosensors have shown success in industries such as clinical, environmental, and food sciences [49-51]. This is in part thanks to the versatility of the material, which has been utilized in electrochemical, physical, and optical biosensors. For the purpose of this thesis, this section will focus specifically on LIG-based electrochemical immunosensors.

You et al, reported an interdigitated LIG electrode sensor decorated with gold nanoparticles (AuNPs), for the impedimetric of the detection of *Escherichia coli* O157:H7. A gold chitosan hydrogel ink was blade coated on a polyimide film and subsequently laser scribed into an interdigitated electrode design. A goat anti-*E coli* O157:H7 antibody solution was dropcasted on the surface followed by dropcasting of BSA to block nonspecific adsorption. Detection was performed using the R_{ct} values obtained in faradaic EIS. Results indicated a linear range over the tested range ($1x10^2$ to $1x10^8$ cfu/mL) with an LOD of 100 cfu/mL. Additionally the fabricated sensor exhibited flexibility with only a 10% decrease in response after 500 cycles [52]. AuNPs have also been implemented in a LIG based nucleic acid methylation sensor (m6A-RNA and 5mC-ssDNA). The corresponding sulfydryl modified antibodies were immobilized on the AuNPs through the formation of gold-thiol bonds. This was followed by dropcasting of biotinylated-m6A-Ab or biotinylated-5mC-Ab which bonded to the methyl groups of the antibodies. Lastly, the binding of biotin and streptavidin modified HRP is then utilized to introduce HRP, which catalyzes the redox reaction of the H_2O_2 and hydroquinone (HQ) (**Figure 2.5.)** allowing for the detection of the biomolecules. Detection was performed

using DPV and achieved a linear range of 0.01 nM to 10 nM for both targets and an LOD of 2.81 pM for m6A-RNA and 9.53 pM for 5mC-ssDNA [53].

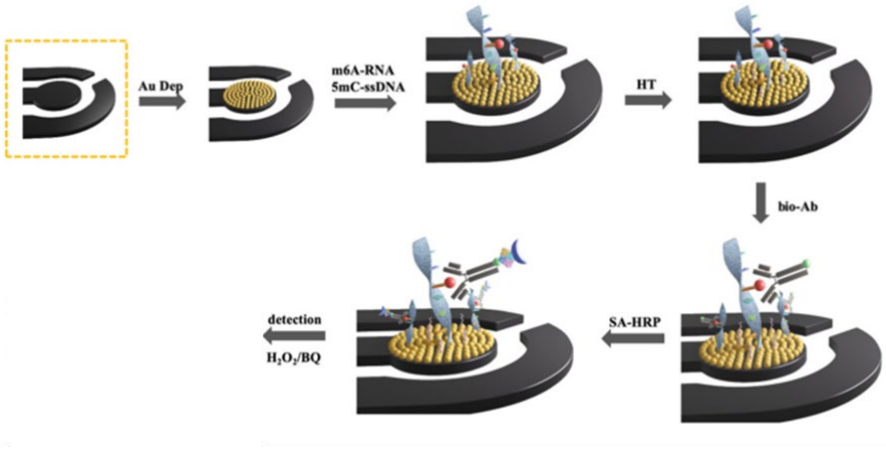

Figure 2.5. Fabrication of the m6A-RNA and 5mC-ssDNA biosensor [53].

LIG have also been utilized for diagnostics in the medical field. For example, in a 2022 article, Oliveira et al. reported a LIG based immunosensor for the detection of SARS-CoV-2 antibodies in blood. The sensor was used with a miniature potentiostat for portability and fast results. Like other immunosensors, EDC/NHS chemistry was used to immobilize chimeric antigens to the LIG which have specific binding towards the SARS-CoV-2 antibodies. The LIG based sensor was able to successfully differentiate patients with and without the SARS-COV-2 infection with a response time of less than three minutes [54]. Another immunosensor with a portable potentiostat was reported for the detection of TNF-α, a cytokine involved in inflammatory responses. The immobilized anti-TNF-α DA catalyzed the oxidation of the 3,3′,5,5′-Tetramethylbenzidine (TMB) substrate by H_2O_2 after binding the streptavidin-HRP to the antibody, creating an

enhanced and measurable current. The Non-faradaic chronoamperometric detection of TNF-α had an LOD of 0.6 pg/mL over a range of 2 pg/mL to 500 pg/mL [55]. LIG have also been utilized for the detection of cancer biomarkers. Interleukin-6 (IL-6) also play a role in the inflammatory process. Tan et al. created a IL-6 voltammetric sensor that achieved an LOD of 5.1 pg/mL IL-6 and a test time of 90 minutes, which is comparable to ELISA kits [56].

Yen et al. used DPV for the detection of alphafetoprotein (AFP) and Carcinoembryonic antigen (CEA). Amine groups and carboxyl functional groups were formed directly on the surface using (3-Aminopropyl)triethoxysilane (APTES) and succinic acid, for the direct bonding of the antibodies. Simultaneous detection of CEA and AFP was performed using two working electrodes that shared a reference and counter electrode. As shown in **Figure 2.6.**, the distinct differences in peak current allowed for the differentiation and detection of the two biomarkers simultaneously [57].

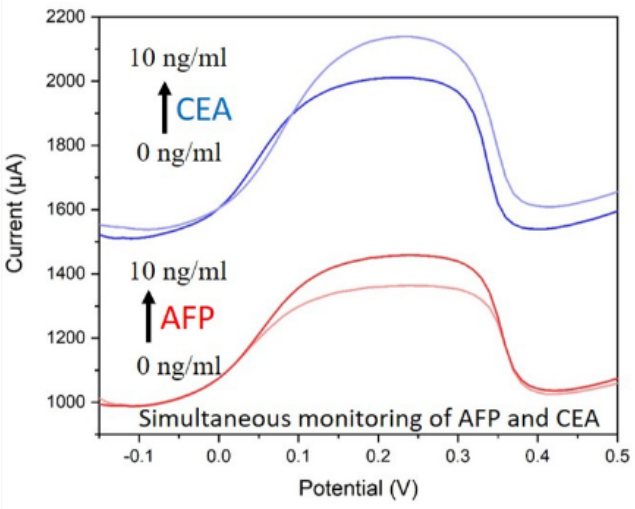

Figure 2.6. DPV diagram of the simultaneous detection of CEA and AFP in PBS [57].

To summarize, the conductivity, flexibility, and functionalization capabilities of laser induced graphene have proved useful in many biosensor applications. The versatile platform allows for potentiometric, amperometric, and impedimetric based immunosensors. Along with their detection abilities, they have shown long term stability and reproducibility which are vital to commercialization and widespread use.

Table 1.2. Summary of LIG-based immunosensors.

Setup	Analyte	Method	Buffer media	Linear range	Limit of detection	Reference
2-electrode faradaic	*Escherichia coli* O157:H7	EIS	PBS	$1x10^2$ - $1x10^8$ cfu/mL	$1x10^2$ cfu/mL	[52]
3-electrode faradaic	m6A-RNA and 5mC-ssDNA	DPV	PBS	0.01 nM - 10 nM (both)	2.81 pM and 9.53 pM	[53]
3-electrode faradaic	SARS-CoV-2 antibodies	DPV	Blood	-	-	[54]
3-electrode non-faradaic	TNF-α	CA	PBS	-	0.6 pg/mL	[55]
3-electrode faradaic	IL-6	CV	PBS	10-500 ng/mL	5.1 pg/mL	[56]
3-electrode faradaic	AFP and CEA	DPV	PBS	0.75 ng/mL – 100 g/mL (both)	13.68 pg/mL and 50.66 pg/mL	[57]

3. Methodology

3.1. Materials

Polyimide (PI) film was purchased from McMaster-Carr (Aurora, OH, USA). Monoclonal anti-cortisol antibody (ab1949) was purchased from Abcam (Cambridge, UK). Gold (III) chloride trihydrate ($HAuCl_4$,) potassium nitrate (KNO_3), 3-Mercaptopropionic acid (3-MPA), N-Hydroxysulfosuccinimide sodium salt (Sulfo-NHS), 1-Ethyl-3-(3-dimethylaminopropyl)carbodiimide (EDC), sodium chloride, potassium phosphate monobasic, and sodium phosphate dibasic dihydrate were purchased from Sigma Aldrich (St. Louis, MO, USA). A 2-(N-morpholino) ethanesulfonic acid (MES) was purchased from Thermo Scientific (Waltham, MA, USA). Bovine serum albumin (BSA) was purchased from VWR (Solon, OH, USA). Potassium hexacyanoferrate (II) trihydrate and potassium hexacyanoferrate (III) were purchased from Alfa Aesar (Ward Hill, MA, USA). All reagents purchased were of analytical grade and used as received without any further purification.

3.2. Optimization of LIG production

To enhance the stability, and reproducibility of the cortisol biosensor, the LIG must be optimized. By obtaining a mechanically stable electrode with low deviation in conductivity, deviations in structure can be minimized, thus improving reproducibility of the cortisol sensor. Dots per inch (DPI) and laser writing direction (x-axis or y-axis) was optimized prior to the power dose assay. Results indicated that 1000 DPI produced the most stable electrode while x-axis lasering showed a slight decrease in resistance

compared to y-axis lasering, thus these conditions were used for the assay. To optimize the LIG, a power dose assay was performed by producing LIG at varying laser power and laser speed to find the laser output parameters that resulted in the most stable and conductive LIG. The electrical line resistance of the samples was measured by two-point measurements using a Fluke 179 digital multimeter (**Figure 3.1.)** and a custom-made probe 1 cm apart from each end point. Measurements were conducted at 1 cm increments starting from the bottom (square end) of the LIG to the top (circular end) and then averaged. Three electrodes were produced at each condition to obtain a standard deviation of the line resistance.

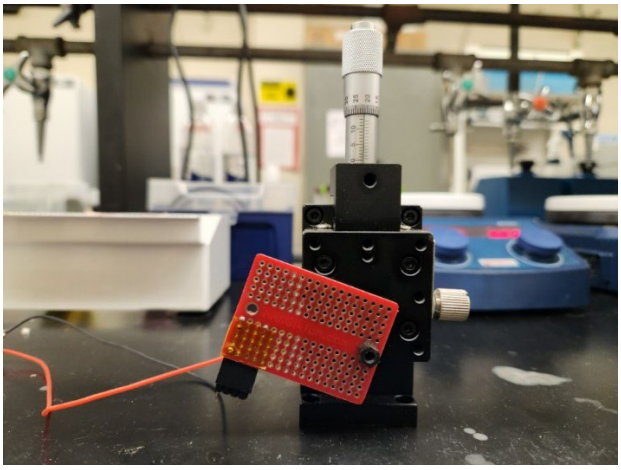

Figure 3.1. Picture of the custom-made probes using precision micrometer stage incorporated with Fluke 179 digital multimeter with 1 cm distance between the probes.

3.3. Construction/surface modification of LIG cortisol biosensor

The LIG electrode was obtained by subjecting PI to a OMTech 40W CO_2 laser cutter/engraver (Anaheim, CA, USA). Adobe illustrator was used to create the design of the IDE and consisted of 10 ‘arms’ with 5 on each side (0.4mm x 7.2 mm) and a 0.5mm

spacing between each arm. The optimized dimensions were obtained by adjusting the length, spacing, and number of arms of the electrode, to obtain the lowest resistance. Once optimized, the Adobe illustrator file was exported to the laser engraving software LightBurn, to communicate with the CO_2 laser.

The procedure of LIG formation is shown in **Figure 3.2.** Prior to construction, the water pump was turned on to keep the tube of the laser cool and the fan of a fume hood was activated to uptake any debris. For the first step of construction, a PI film was cut and taped to a microscopic glass slide to provide a rigid support. After double checking the fan and water pump were on, the glass slide was placed into the CO_2 laser. The top and bottom of the slide were taped to the bed of the laser to further prevent curling of the PI film from the heat of the laser. Finally, the top of the laser was closed and ran for LIG formation. After the LIG formation on the PI film, the LIG/PI film was removed, and the individual electrodes were cut out of the film. The LIG were then rinsed with acetone, 2-propanol, and ethanol, to remove any impurities.

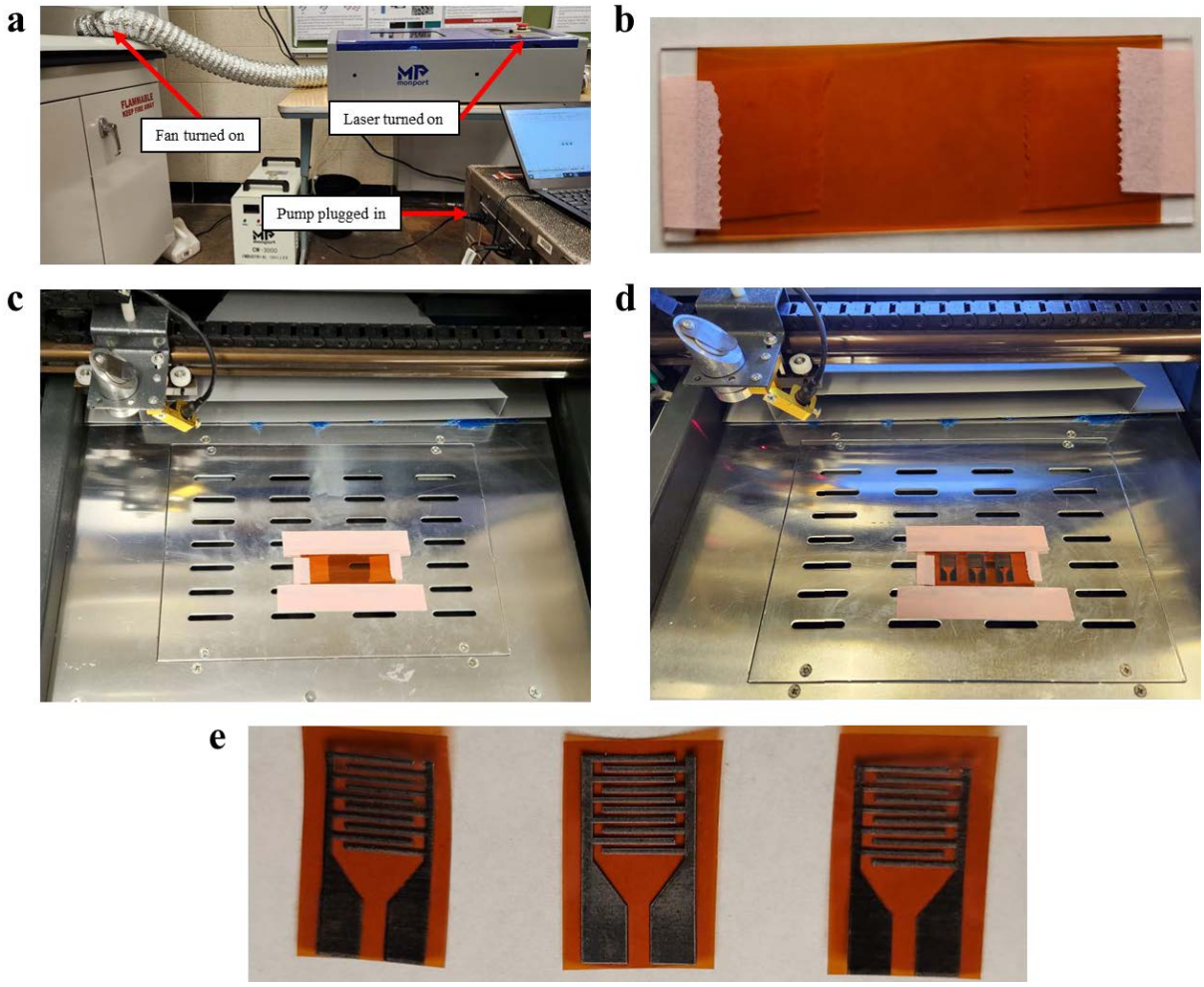

Figure 3.2. Step by step procedure of LIG formation. (a) Plugging in the water pump, turning on the fan, and the laser. (b) Taping the cut PI film to a glass slide. (c) Taping it to the bed of the laser and the laser is turned on. (d) LIG is formed. (e) The tape is removed and the LIG are individually cut out.

To increase wettability of the LIG, it was placed into a Harrick PDC-32G Plasma Cleaner (Ithaca, NY, USA) for oxygen plasma treatment **Figure 3.3.** [58]. Prior to treatment, a pump was run for 3 minutes to create a vacuum in the chamber. Then the

system was turned on and the RF level was set to high for 30 seconds and then the vacuum was slowly released.

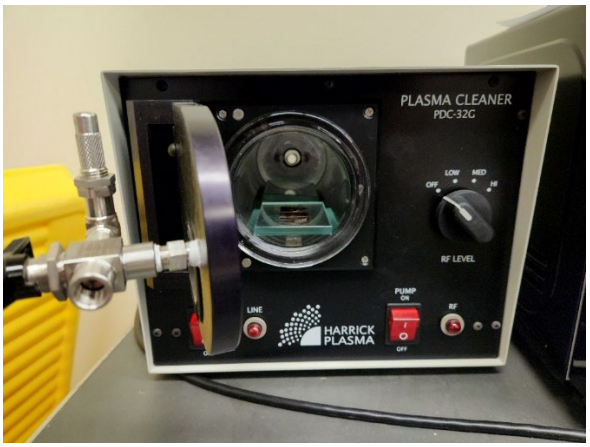

Figure 3.3. Plasma cleaner with the LIG inside prior to treatment.

Thin copper tape was measured and cut into 2 cm lengths. Then the copper tape was removed from the plastic backing by carefully peeling back with tweezers. Then, the tape was gently placed over both connection points and pressed down to ensure full contact with the LIG. This purpose of this step is to avoid fracturing of the LIG from the alligator clips when performing characterization or detection experiments.

This was followed by the insulation of the body of the electrode using a 5-minute epoxy from Devcon Home (Solon, OH, USA). Each solution of the epoxy was measured out equally and mixed vigorously to ensure homogeneity. Then, using a 10 µL pipette tip, the body of the electrode was carefully covered (**Figure 3.4.(a)**). The electrodes were placed into a vacuum chamber for 5 minutes (**Figure 3.4.(b)**) to remove any air pockets under the epoxy and allowed to fully cure for 3 hours.

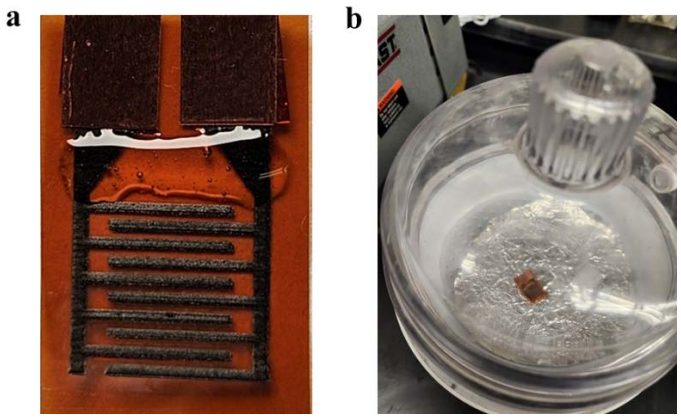

Figure 3.4. (a) LIG with the insulation layer placed on the body of the electrode and (b) the vacuum chamber used to remove air bubbles from the epoxy.

To obtain the gold nanoparticle (AuNP) modified laser induced graphene (LIG) electrode, AuNP were electrochemically deposited on the LIG surface via cyclic voltammetry (CV) over the potential range of -0.2 V to -1.4 V at a scan rate of 50 mV/s for 10 cycles in a 1 mM $HAuCl_4$ in 0.1 M KNO_3 solution [59, 60]. Deposition was achieved in a 3-electrode system with the IDE as the WE, SCE as the RE, and platinum wire as the CE (**Figure 3.5.**). The working electrode of the Gamry was connected to both copper taped connection points of the IDE, allowing for gold nanoparticle deposition on each side.

Figure 3.5. 3-electrode setup for AuNP electrodeposition.

After the tenth cycle the CV stabilized (**Figure 3.6.**), hence it was chosen for the cycle limit [61]. After electrodeposition, the AuNP-LIG was thoroughly washed with DI water to remove unstable AuNPs and any of the remaining solution, then allowed to air dry.

To immobilize anti-cortisol antibody on the AuNP sites on the LIG electrode, thiol chemistry was used. First, a self-assembled monolayer of MPA was formed on the AuNP by incubating the LIG in a 10 mM MPA in ethanol for 1 hour at room temperature followed by a rinse with ethanol and DI water to remove any unbound MPA. Next, the terminal carboxylic acid groups of the MPA were activated to immobilize anti-cortisol antibody. Activation was performed through incubation in a 0.1 M MES buffer containing 40 mM EDC and 100 mM Sulfo-NHS for 1 hour at room temperature. To obtain the antibody immobilized AuNP-LIG electrode, the activated electrode was incubated in an anti-cortisol antibody (ab) solution at 5 µg/mL in 10 mM Phosphate-buffered saline (1x PBS, pH 7.4) for 2 hours. The antibody modified electrode was then

gently rinsed with PBS to remove unbounded antibody. To minimize undesired unspecific adsorption on the surface of the LIG, the electrode was incubated in a 1% bovine serum albumin (BSA) in 10 mM PBS. The BSA/ab/EDC-NHS/AuNP/LIG modified electrode was rinsed with PBS to remove any unbound BSA and subsequently stored in a sealed tube containing PBS at 4°C until further use.

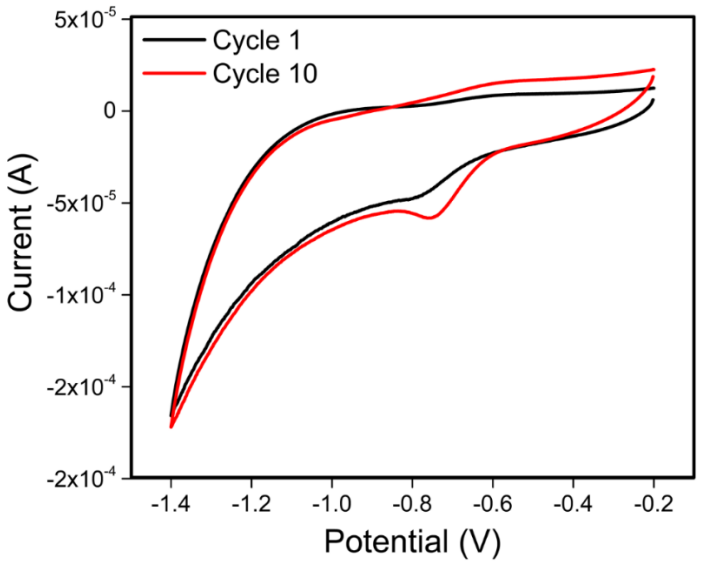

Figure 3.6. Electrodeposition of AuNPs on LIG electrode (first and last cycle).

All rinsing steps were conducted by submerging the LIG in a 10 mL beaker of the rinsing solution. This was repeated three times, for a total of 90 seconds. Additionally, all incubation steps were carried out in a 10 mL centrifuge tube (**Figure 3.7.(a)**). To avoid corrosion of copper contact points, the IDE were placed in an empty centrifuge followed by the pipetting of the solution up until the epoxy insulating layer (**Figure 3.7.(b)**).

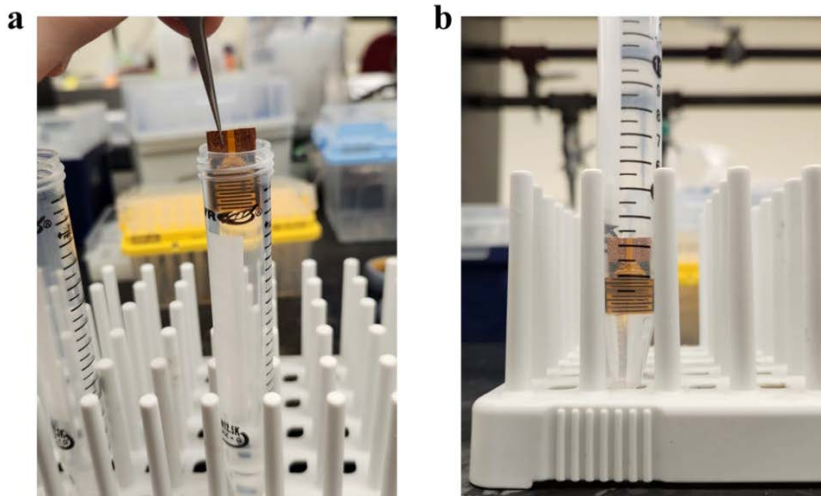

Figure 3.7. (a) Rinsing step performed between each surface modification and (b) the incubation step in a centrifuge tube.

3.4. Characterization of LIG cortisol biosensor

Physical, chemical, and electrical properties of the modified electrodes were characterized using scanning electron microscopy (SEM), energy dispersive X-ray spectroscopy (EDX), X-ray powder diffraction (XRD), Raman spectroscopy, FT-IR, and EIS.

The JIB-4500 MultiBeam integrated with SEM-EDX (JEOL, Japan) was used for SEM imaging and EDX analysis on LIG and AuNP/LIG. SEM images were collected at an electron energy of 15kV for 15,000x, 500x, and 100x magnifications for morphology characterization and verification of the electrodeposition of AuNPs. EDX characterization was carried out at 5000x magnification with an electron energy of 138 eV for the elemental analysis of the LIG and AuNP/LIG.

XRD was performed with a Bruker X8 Prospector Ultra (Billerica, MA, USA) via Cu radiation to characterize the structures of the samples. The XRD spectra of PI film,

LIG, and AuNP were obtained, and the peaks were analyzed to show the degree of graphitization and defect after formation of the graphitic structure, and further verify the presence of electrodeposited AuNP on the LIG surface.

Raman spectroscopy is a commonly used technique to examine chemical structure and crystallinity. In this case, it was used to examine the degree of graphitization and verify the presence of the AuNPs. Raman spectra were collected using a Horiba iHR320 spectrophotometer (Horiba, Japan) at 531.4 nm laser with a 1800g/mm diffraction gratings. The system was first turned on and calibrated. Raman spectroscopy were obtained in this fashion for LIG and AuNP/LIG.

The Perkin Elmer Spectrum 100 FT-IR spectrophotometer (Waltham, MA, USA) was used to conduct FT-IR spectroscopy on various samples including bare LIG, AuNP/LIG, EDC-NHS/AuNP/LIG, ab/EDC-NHS/AuNP/LIG, and BSA/ab/EDC-NHS/AuNP/LIG. These samples were analyzed against a KBr background. To prepare the KBr-LIG palate, KBr and LIG were mixed in a ratio of 100:1. The following mixture was then pressed with a Pike KBr bolt press to form a solid mass. The study examined the intensity of light transmitted between 400-4000 cm^{-1} for 16 scans.

To verify the LIG IDE underwent surface modification, EIS was performed with a Gamry Interface 1010E Potentiostat (Warminster, PA, USA) using A two-electrode system consisting of the LIG IDE. The EIS measurements were carried out in 5 mM $Fe(CN)^{3-}/Fe(CN)^{4-}$ PBS solution as a supporting electrolyte. 10 mL of the redox containing PBS was measured and poured into a 15 mL beaker. To set up the two-electrode system, the working sense and working electrode of the Gamry system were coupled, as well as the reference and counter electrode. The two coupled electrodes were

placed carefully on the connection points of the LIG and submerged in solution up to the insulating layer. The potentiostat was then turned on and Impedance spectra were collected in the frequency range from 1 Hz to 100 kHz with a potential amplitude of 10 mV rms at 10 points per decade. Parameters of the electrical equivalent circuit were obtained by fitting the impedance function to the measured Bode and Nyquist plots with a complex nonlinear least square (CNLS) program built in the Gamry Echem Analyst 2 (ver. 7.10). The electron transfer resistance (R_{ct}) was obtained from the model to compare the differences at each step of modification.

EIS is an effective and non-destructive method for characterizing the interfacial electrical properties of modified surfaces of electrodes [62]. EIS data comprises both imaginary and real impedance components over a specified range of frequencies. Fitting the impedance spectrum with an equivalent circuit model, allows for the estimation of parameters such as double-layer capacitance, solution resistance, charge transfer resistance, and diffusion impedance [63]. Performing EIS in a faradaic solution allows for the determination of the resistance produced by the redox solution reacting and transferring electrons, commonly known as the electron charge transfer resistance (R_{ct}). Changes on the surface that impede redox reactions, such as antibody-antigen binding events that cover the surface of an electrode, will increase the R_{ct} [64]. Therefore, the R_{ct} may be utilized to verify each stage of surface modification was successful.

3.5. Cortisol detection

To examine the performance of the sensor, non-faradaic cortisol detection was conducted in a 10 mM PBS solution spiked with increasing cortisol concentrations (0.1

pM-100 nM). The cortisol solution was prepared using a serial dilution technique in 1.5 mL centrifuge tubes at a concentration ten thousand times higher than needed, due to using 10 µL injections in a 10 mL solution. Briefly, the 100 nM solution was prepared first. Then, 900 µL of PBS was placed in separate tubes for each concentration. 100 µL of the 100 nM solution was transferred into the next tube, thus diluting it ten times to 10 nM. This step was repeated all the way down to 0.1 pM. The following solutions were placed into the refrigerator until needed for detection. Cortisol solutions were prepared every two weeks to keep the solutions fresh.

First, 10 mL of 10 mM PBS was measured using a 15 mL pipette and transferred into a 15 mL beaker, followed by connecting the working/working sense electrode and counter/reference electrode to the connection points of the fully modified electrode. Injections started at 0.1 pM concentration up to 100 nM. 10 µL injections were injected and 30 minutes after each injection of cortisol, EIS was performed and Z_{mod} values at 200 Hz were collected at each concentration. The Z_{mod} values were used to create a calibration plot in terms of the percent change at each concentration compared to the base level (no cortisol injected). The electrochemical cell for cortisol detection is depicted in **Figure 3.8.**

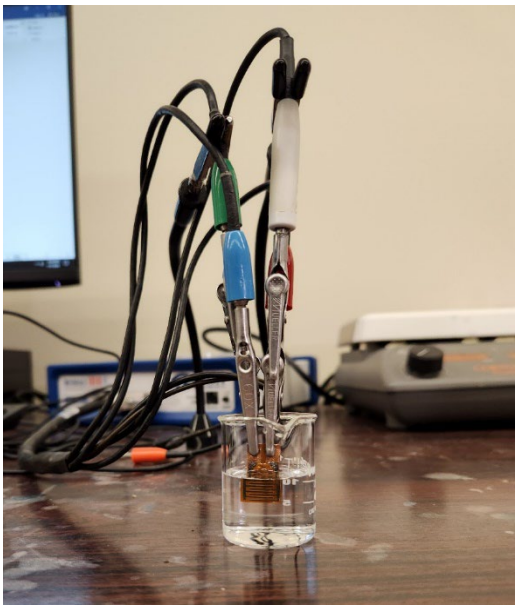

Figure 3.8. Electrochemical cell setup for cortisol detection.

3.6. Specificity

Specificity of the fully modified electrode (BSA/ab/EDC-NHS/AuNP/LIG) was conducted through a cross-reactivity in a PBS solution containing testosterone, cortisone, and 17-hydroxyprogesterone (17-OHP). They are known to have similar structures to cortisol, making them prime candidates for assessing the binding specificity of the biosensor [65-67]. EIS measurements were obtained prior to the 100 nM injection of the interfactant, and 30 minutes after the injection. The percent change in Z_{mod} of each interfactant (n=3) was compared to the response after a 100 nM injection of cortisol. The response of the sensor to interfactants was then compared to cortisol to evaluate the specificity.

3.7. Cortisol detection in synthetic sweat

Various interferent molecules are found in human sweat, which may impact the electrochemical response. To examine the effect of sweat-based interferents, cortisol dose response from 0.1 pM to 100 nM was performed in a synthetic sweat solution containing commonly found sweat based interferents; 84 μM creatinine, 10 μM ascorbic acid, 0.17 mM glucose, and 59 μM uric acid [68]. Detection was performed using the same procedure described in the cortisol detection section.

3.8. Reproducibility

Reproducibility tests are an excellent way to determine the feasibility of a sensor in real world applications. A large variation in sensor performance makes calibration nearly impossible rendering it useless. To examine the efficacy of the modified electrode, reproducibility was performed by independently preparing five BSA/ab/AuNP/LIG. The sensors were then placed in the detection set up used for cortisol detection. EIS was performed prior to a 100 nM injection of cortisol and 30 minutes after. The resulting percent change in Z_{mod} was found for each electrode and the percent of relative standard deviation (%RSD) was calculated.

3.9. Repeatability

To evaluate the consistency of the LIG sensor, replicant measurements were performed under the experimental conditions for cortisol dose response. The repeatability of the BSA/ab/AuNP/LIG electrode was investigated by running EIS three times at each

concentration (0.1 pM-100 nM). The percent relative standard deviation (%RSD) of the Z_{mod} at 200 Hz was then calculated for each concentration.

4. Results and Discussion

4.1. Optimization of LIG production

Figure 4.1. indicates the line resistance of each LIG produced with the CO_2 laser operating at 1000 dots per inch (DPI) in the X-direction with varying power (W) and speed (mm/s). The assay indicated that a power output of 24 W and laser speed of 70 mm/s produced the lowest resistance of 87.4 ± 0.27 Ω/cm. The standard deviation (n=3) of each parameter was also examined to determine the most reproducible condition. Additionally, the condition had little flaked fragments, which can cause breakage during modification. The optimized parameters resulted in the highest conductivity and the lowest standard deviation, and stability, indicating high reproducibility. Therefore, LIG produced at these parameters were used for the remainder of the study.

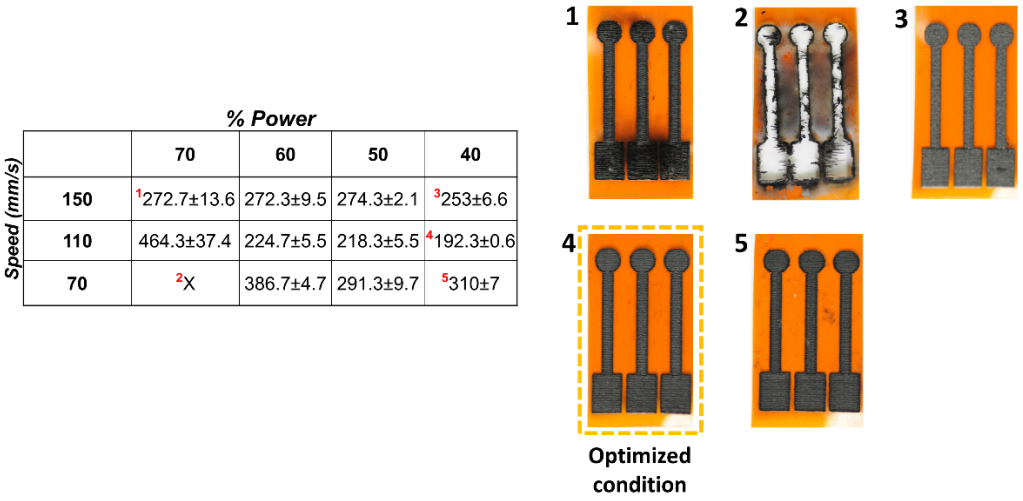

% Power

Speed (mm/s)	70	60	50	40
150	[1]272.7±13.6	272.3±9.5	274.3±2.1	[3]253±6.6
110	464.3±37.4	224.7±5.5	218.3±5.5	[4]192.3±0.6
70	[2]X	386.7±4.7	291.3±9.7	[5]310±7

Figure 4.1. Power dose assay for LIG optimization.

4.2. Characterization of LIG cortisol biosensor

4.2.1. XRD analysis

X-ray diffraction (XRD) was applied to confirm graphene-like material formation followed by AuNPs on the LIG electrode (**Figure 4.2.**) LIG exhibited a short peak at ~26° which is attributed to low crystallinity and low diffraction [69]. The AuNP/LIG exhibited reflections of Au face-centered cubic crystallographic structure (38°, 44°, 64°, and 77°) signifying AuNP were successfully deposited on the LIG electrode surface [70, 71]. The short peak observed at ~26° is indicative of a highly graphitized surface, thus increasing the surface area and consequently the available bonding sites for reagents.

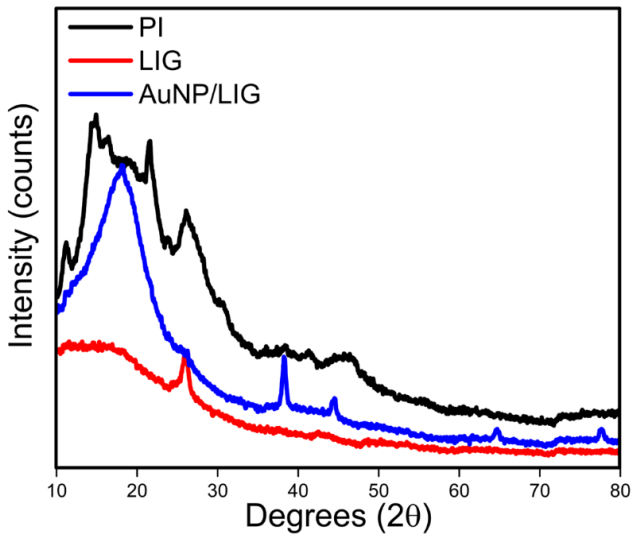

Figure 4.2. XRD spectra of PI, LIG, and AuNP/LIG.

4.2.2. SEM-EDX

The surface morphology of the LIG and AuNP/LIG electrodes were examined through SEM imaging at various magnifications with further analysis of the elemental

composition achieved by EDX for both LIG (**Figure 4.3.(a-c))** and AuNP/LIG (**Figure 4.3.(d-f)).** The porous 3D structure of LIG and AuNP/LIG is clearly visible. Bright spots were found after the formation of AuNPs via electrodeposition (**Figure 4.3.(d-f))**. Through the CV electrodeposition technique, AuNPs were formed on the LIG electrode surface with a higher density on the edges of the pores. Furthermore, at 100x magnification, the linear pathway of the CO_2 laser is visible through the tightly packed ridges. A change in overall brightness between the LIG and AuNP/LIG is most visible at the 100x and 500x magnification, this change in brightness is due to the AuNP's high conductivity providing a more accurate representation of the structure of the LIG. The porous 3d structure provides a large surface area for the attachment of more AuNP's, thus increasing conductivity. Moreover, the increase in AuNP density provides a large surface area for contacting more reagents. Therefore, the resulting AuNP/LIG enhances cortisol detection. Results from EDX characterization for LIG and AuNP/LIG are shown in **Figure 4.4.** The fabricated LIG is comprised of 100 wt% carbon with AuNP/LIG comprised of 93.54 wt% carbon with the remaining 6.46 wt% gold, further confirming successful electrodeposition of AuNPs on the LIG surface. The absence of other elemental peaks indicates a pristine surface with undetectable traces of contaminants. To obtain higher counts per minute, EDX analysis was ran at low resolution (138eV) which can cause the overlapping of elemental peaks [72]. However, no such overlapping was observed for the LIG or AuNP/LIG electrodes.

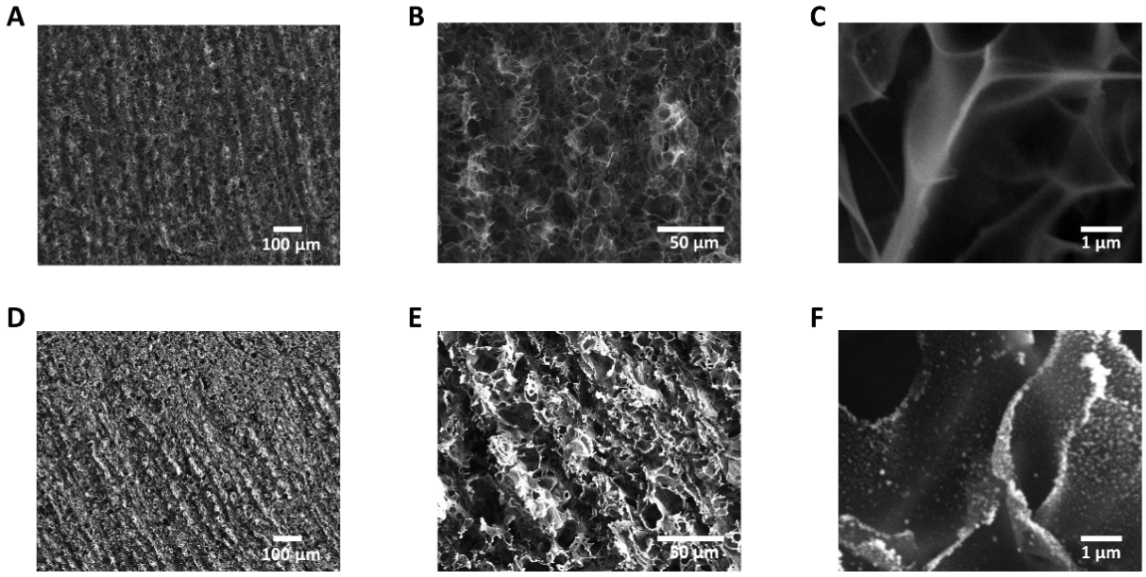

Figure 4.3. SEM images of (a-c) LIG and (d-f) AuNP-LIG electrodes respectively**.**

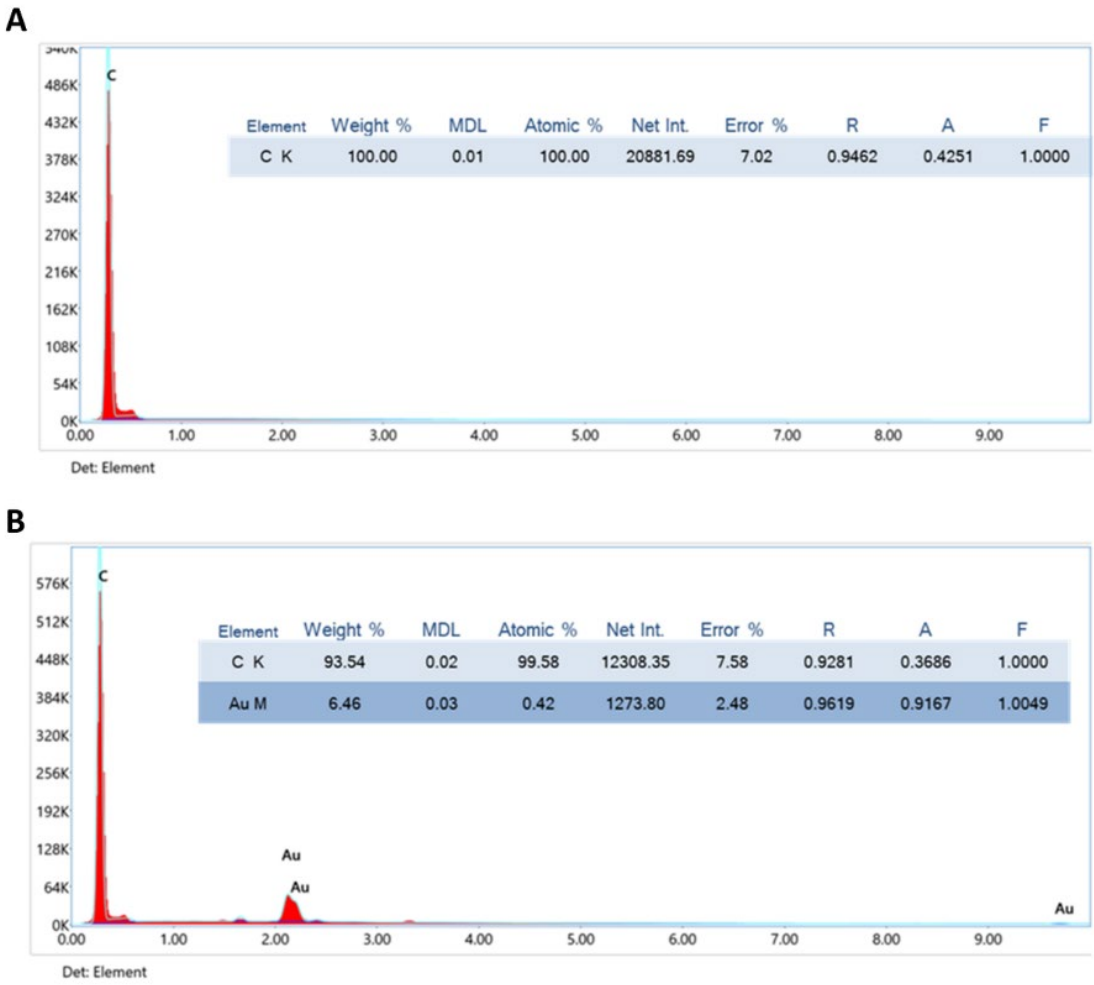

Figure 4.4. EDX spectra of (a) bare LIG and (b) AuNP/LIG electrodes.

4.2.3. FT-IR

FT-IR analysis was performed with the intensity of light transmitted in the range of 400-4000 cm^{-1}, which provides information about the molecular vibrations and functional groups present in the samples. By comparing the FT-IR spectra of the different samples, it is possible to identify any changes in the molecular structure and composition [73]. The FT-IR peaks after successive modification of the bare LIG showed different compositions, shown in **Figure 4.5.** The interaction of AuNP with amid group of the LIG

was confirmed by the presence of a C-O bond at 1100 cm^{-1} in AuNP/LIG [74]. Additionally, Au-O peak was seen at 616 cm^{-1} [73, 75]. Moreover, the immobilized antibody on the AuNP sites and BSA blocking the LIG background were proved by FT-IR, which is denoted by the presence of the O-H and N -H bond as indicated by hump at 3444 cm^{-1} [76, 77]. Anti-cortisol antibody and BSA protein are macro biomolecules that exhibit transmittance spectra at approximately 1600 cm^{-1}, which corresponds to the N-H and O-H vibrational stretching bonds of the amide I, amide II, and amide III bonds at 1650, 1540, and 1450 cm^{-1}, respectively [78]. The peaks of both ab/EDC-NHS/AuNP/LIG and BSA/ab/EDC-NHS/AuNP/LIG electrodes were observed at 1660 cm^{-1}, 1553 cm^{-1}, and 1440 cm^{-1}, indicating that the amide I, amide II and amide III are present, and the surface modification was successfully performed. The modified electrode BSA along with the C-H stretching vibration with the presence of peaks between 2920-2870 cm^{-1}. The samples of ab/EDC-NHS/AuNP/LIG and BSA/ab/EDC-NHS/AuNP/LIG exhibited peaks related to the presence of antibodies and BSA on the graphene surface, respectively, with peaks at 1550-1600 cm^{-1} confirming the presence of C-C stretching and amide I, amide II, and amide III peaks at 1650-1700 cm^{-1} [79, 80]. The samples of ab/EDC-NHS/AuNP/LIG and BSA/ab/EDC-NHS/AuNP/LIG exhibited peaks related to the presence of antibodies and BSA on the graphene surface, respectively, with peaks at 1550-1600 cm^{-1} confirming the presence of C-C stretching and amide I, amide II, and amide III peaks at 1650-1700 cm^{-1} [81, 82].

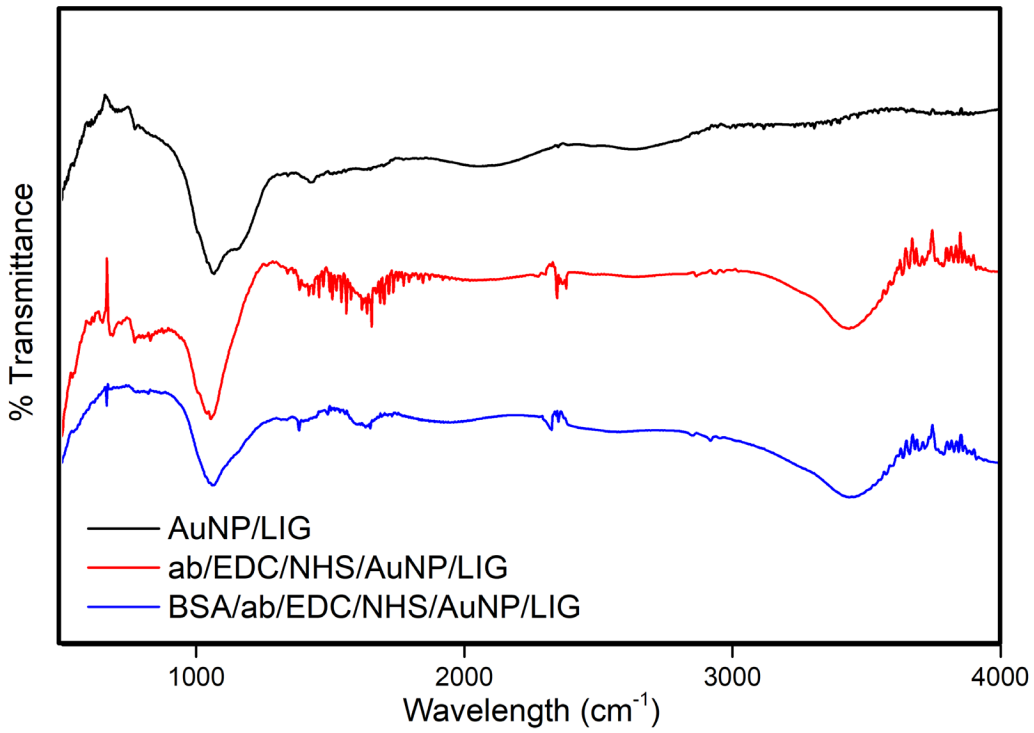

Figure 4.5. FT-IR spectra of, AuNP/LIG, ab/EDC-NHS/AuNP/LIG and BSA/ab/EDC-NHS/AuNP/LIG electrode samples.

4.2.4. Raman spectroscopy

Raman spectroscopy was performed to examine the graphitic structure of the LIG electrode. It is particularly useful in determining the degree of disorder in the sp^2 carbon lattice [83]. Raman spectra of LIG and AuNP/LIG have both D (defect states) and G (graphitic states) bands at around 1350 cm^{-1} and 1590 cm^{-1} respectively (**Figure 4.6.**). The intensity ratio, I_D/I_G, represents the degree of graphitization that occurred, and was found to be 0.475 and 0.548 for LIG and AuNP/LIG. The increase in intensity is the result of interactions between the AuNPs and graphene surface. Specifically, the presence of the AuNPs increased the disorder of the graphitic structure [84].

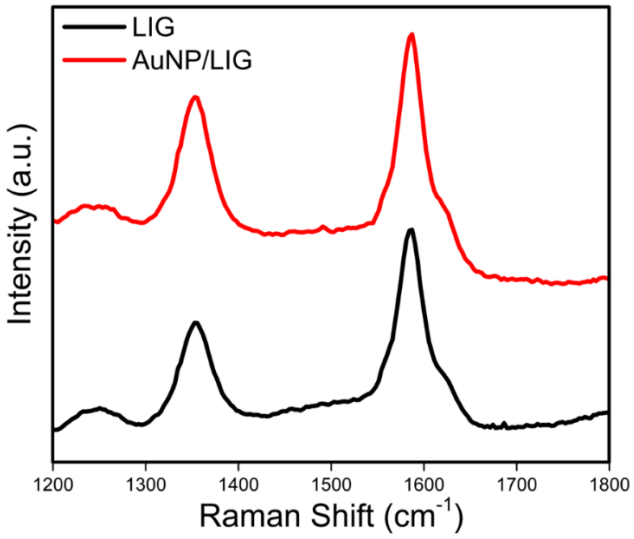

Figure 4.6. Raman spectra of PI, LIG, and AuNP/LIG.

4.2.5. Electrochemical impedance spectroscopy (EIS)

The electrochemical characterization of the different electrodes (LIG, AuNP/LIG, Ab/AuNP/LIG, and BSA/Ab/AuNP/LIG) was carried out using EIS from 1-10,000 Hz with a 10 mV rms perturbation and 0 V (DC). All measurements were performed in a redox solution composed of PBS and 5 mM $(Fe(CN)_6)^{3-}/(Fe(CN)_6)^{4-}$ (1:1) solution with the equivalent model shown in **Figure 4.7. insert**. At high frequencies, electron charge transfer is prominent as evident by the semi-circle portion of the Nyquist plot. At lower frequencies, diffusion is dominant resulting in an increase in Warburg impedance as depicted by the diffusion tail in the Nyquist plot [62]. The data was fit with a modified Randles circuit and R_{ct} was obtained. The AuNP/LIG electrode showed the lowest R_{ct} ($30.98 \pm 3.59\Omega$), indicating electrodeposition of AuNP effectively increased the conductivity of the surface. Following the AuNP/LIG, EDC-NHS/AuNP saw an increase with a R_{ct} of $34.83 \pm 7.38\Omega$. The increase can be attributed to the self-assembled

monolayers (SAM) immobilization of 3-MPA to the AuNPs, which inhibits the electrolyte/electrode charge transfer. After 3-MPA activation via EDC/NHS, incubation of the anti-cortisol antibody saw an increase of 144% (46.32 ± 2.43), signifying the bonding of large amounts of the antibody to the surface, further impeding charge transfer to the electrode. All steps leading to antibody immobilization resulted in a lower R_{ct} than the bare LIG (50.42 ± 11.02), further supporting AuNP electrodeposition effectively increased the sensors overall conductivity, thus improving its overall sensitivity and functionality. Finally, the addition of the blocking agent BSA to the Ab/AuNP/LIG saw a further 168% increase in R_{ct} (77.84 ± 4.04) indicating a large portion of the unmodified surface was successfully covered.

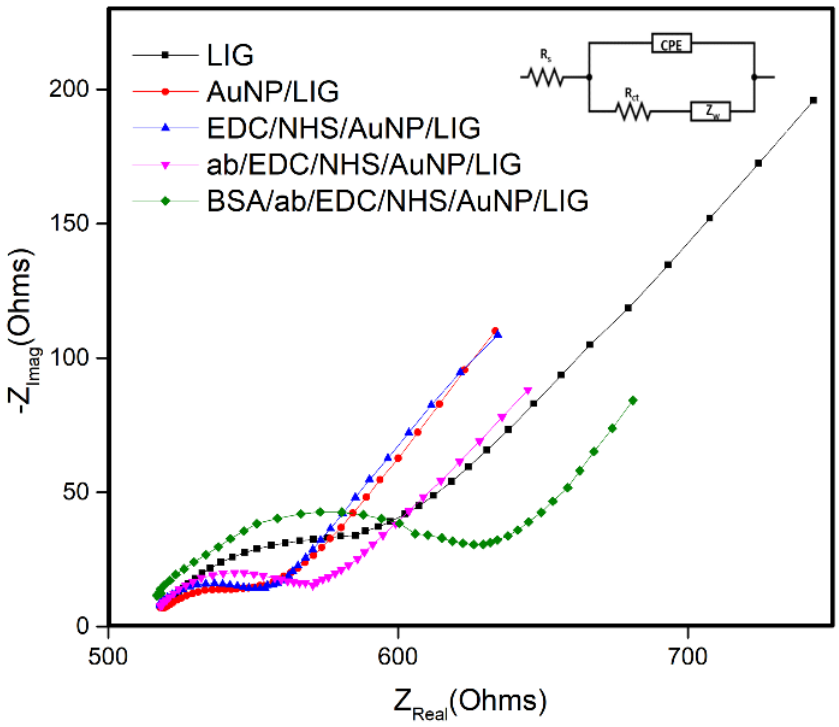

Figure 4.7. Nyquist plot obtained after surface modification procedures (n=3).

4.3. Cortisol detection

Non-faradaic cortisol detection was conducted in a 10 mM PBS solution spiked with increasing cortisol concentrations (0.1 pM-100 nM). 30 minutes after each injection of cortisol, EIS was performed and Z_{mod} values at 200 Hz were collected at each concentration.

Non-faradaic cortisol detection was conducted in a 10 mM PBS solution spiked with increasing cortisol concentrations (0.1 pM-100 nM). The electrochemical cell consisted of the fully modified BSA/Ab/EDC-NHS/AuNP/LIG IDE electrode. 30 minutes after each injection of cortisol, EIS was performed and the Z_{mod} values at 200 Hz were collected at each concentration for calibration. All EIS measurements were performed in the frequency range from 1 Hz to 100 kHz with a potential amplitude of 10 mV rms at 10 points per decade.

A modified Randles circuit model was fit to the EIS data to obtain the electrical characteristics of the system (**Figure 4.8.(a) inset**). R_s represents the solution resistance and is parallel to the C_{LIG} and R_{LIG} in parallel, which is in series with a second circuit containing CPE_{dl} and R_{ct} in parallel. The constant phase element (CPE_{dl}) represents the electric double layer capacitance of the system. CPE_{dl} was used to account for non-ideal conditions such as the surface roughness of the LIG, and uneven ion adsorption onto the electrode surface, allowing for a better representation of the electric double layer capacitance [85, 86].

The resulting Nyquist plot, Bode plot, and model data obtained from cortisol detection are presented in **Figure 4.8.(a)**, **Figure 4.8.(b) ,** and **Table 4.1.** respectively. As cortisol concentration increases, more antibody-antigen complexes are formed within the

electric double layer (EDL). The formation of complexes increases the double layer capacitance (CPE_{dl}), causing the decrease in Z_{Real} observed in **Figure 4.8.(a)** [40]. Furthermore, the bode plot (**Figure 4.8.(b)**) exhibited a consistent decrease in impedance for increasing cortisol levels. This phenomenon is exclusive to non-faradaic EIS, where the absence of redox reactions eliminates the parameters in the Randles model associated with electron transfer, such as (R_{ct}) and Warburg impedance (Z_w), as these become negligible. Consequently, in a non-faradaic system, the impedance is inversely proportional to the electrical double layer capacitance [33]. Therefore, the observed decrease in impedance and corresponding increase in CPE_{dl} (**Table 4.1.**) can be attributed to the interaction of cortisol with the modified electrode surface. Due to the morphology of the LIG $\alpha_{CPE\text{-}LIG}$ and $\alpha_{CPE\text{-}dl}$ values were ~0.5, indicating surface roughness (**Table 4.1.**). The mechanism of the system is further validated through the increase of capacitance values of the circuit (CPE_{dl} and CPE_{LIG}) by 633% and 207%. Additionally a slight decrease in R_{LIG} is observed due to an accumilation of charge on the conductive LIG surface.

To obtain a calibration curve, the percent change in Z_{mod} (200 Hz) was calculated at each concentration with respect to the baseline measurement. A 200 Hz frequency was used because it lies in the range of 5-1000 Hz, which is known to represent the electric double layer capacitance [87]. The resulting cortisol dose response is depicted in **Figure 4.8.(c)**. The sensor exhibited a linear fit (log(Concentration)) over the entirety of the tested range with a high goodness of fit (R^2=0.97) and a LOD (3σ/S) of 0.0085 nM. Overall, the developed cortisol biosensor exhibited a linear range and LOD comparable to previous works (**Table 4.2.**) [40, 41, 45, 47].

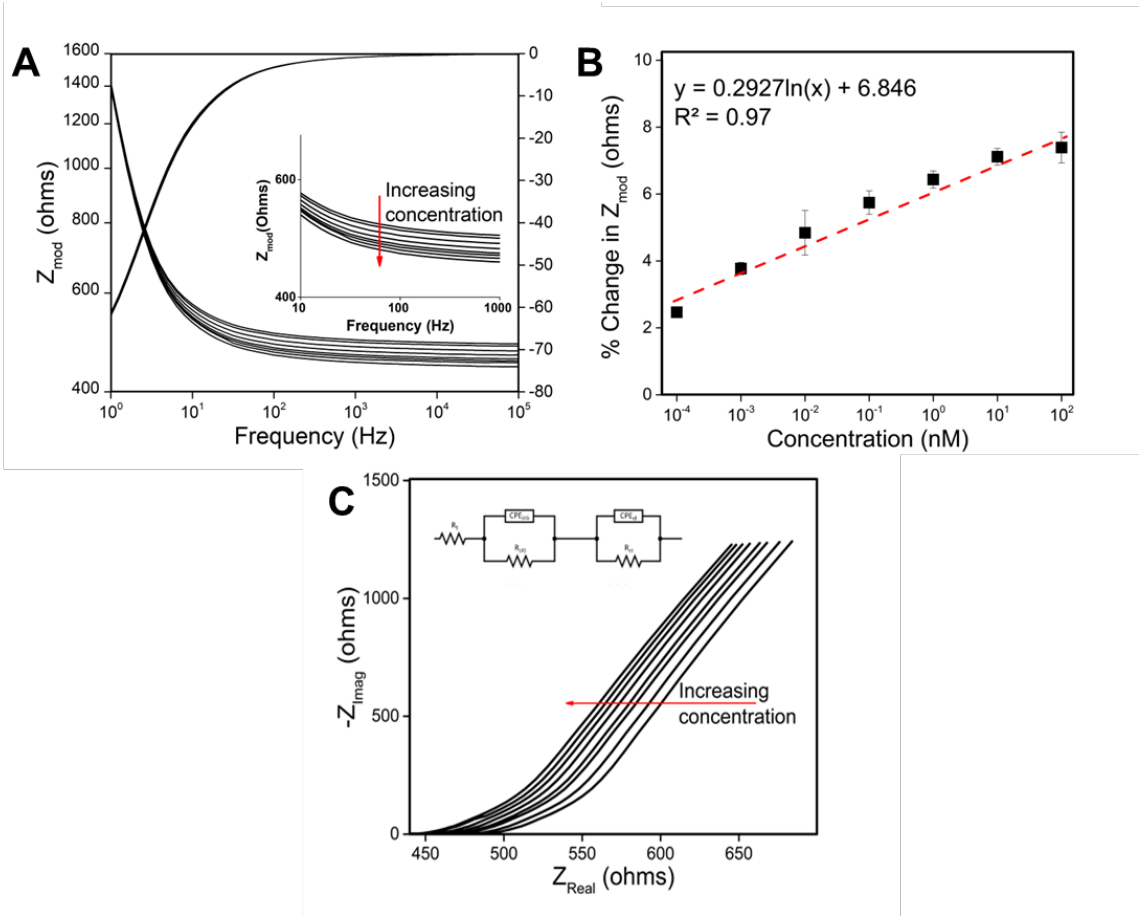

Figure 4.8. (a) Nyquist plot and (b) Bode plot for increasing cortisol concentrations. (c) Cortisol dose response.

Table 4.1. Parameters of modified Randles circuit for increasing cortisol concentration.

	0.1 pM	**1 pM**	**10 pM**	**100 pM**	**1 nM**	**10 nM**	**100 nM**
CPE_{dl}	1.42E-04 ± 3.33E-06	2.41E-04 ± 2.06E-04	2.67E-04 ± 2.27E-04	5.22E-04 ± 6.59E-04	6.72E-04 ± 6.62E-04	7.67E-04 ± 4.37E-04	8.99E-04 ± 3.84E-04
$\alpha_{CPE\text{-}dl}$	4.78E-01 ± 7.07E-02	4.60E-01 ± 1.03E-01	4.61E-01 ± 8.28E-02	3.78E-01 ± 1.56E-02	4.54E-01 ± 1.42E-01	5.88E-01 ± 5.15E-02	4.65E-01 ± 9.32E-02
CPE_{LIG}	2.00E-04 ± 2.60E-04	2.17E-04 ± 2.71E-04	2.95E-04 ± 4.83E-04	3.07E-04 ± 1.63E-04	3.22E-04 ± 1.37E-04	4.09E-04 ± 3.74E-04	4.15E-04 ± 6.21E-04
$\alpha_{CPE\text{-}LIG}$	4.59E-01 ± 6.08E-02	4.98E-01 ± 2.89E-02	5.04E-01 ± 1.37E-01	4.52E-01 ± 8.22E-02	5.20E-01 ± 9.90E-02	4.84E-01 ± 1.19E-01	7.47E-01 ± 3.58E-01
R_s	5.99E+02 ± 3.52E+01	5.83E+02 ± 2.88E+01	5.80E+02 ± 2.79E+01	5.75E+02 ± 2.68E+01	5.71E+02 ± 2.54E+01	5.69E+02 ± 2.51E+01	5.66E+02 ± 2.42E+01
R_{ct}	1.63E+04 ± 2.74E+04	1.92E+04 ± 2.71E+04	2.45E+04 ± 2.46E+04	3.27E+04 ± 1.32E+03	3.30E+04 ± 6.75E+02	3.44E+04 ± 1.06E+04	4.29E+04 ± 2.01E+04
R_{LIG}	2.74E+04 ± 2.57E+04	2.70E+04 ± 4.26E+03	2.65E+04 ± 8.66E+03	2.64E+04 ± 3.00E+04	2.44E+04 ± 1.93E+04	2.26E+04 ± 2.68E+04	2.15E+04 ± 1.45E+04

Table 4.2. Comparison of cortisol biosensors.

Substrate	Setup	Method	Param. used	Buffer media	Linear range	Limit of Detection	Reference
MoS_2 Nanosheet on flexible nanoporous membrane	2- electrode non-faradaic	EIS	|Z| @ 100Hz	Human Sweat	1-500 ng/mL	1 ng/mL	[40]
bifunctional protein interlayer-rGO	3-electrode faradaic	EIS	R_{ct}	PBS	10 pM-100nM	0.0287 ng/mL	[47]
3D Au nanostructured modified PDMS electrode	2-electrode faradaic	EIS	$R_{et,\ Sensor}$	PBS	1pg/ml to 10 ng	0.001 ng/mL	[41]
Au surface conjugated with methylene blue	3-electrode non-faradaic	SWV	µA	PBS	0.05-100 ng/mL	0.05 ng/mL	[45]
AuNP modified LIG	2-electrode non-faradaic	EIS	Z_{mod} @ 200 Hz	PBS	0.1 pM-100 nM	0.00308 ng/mL	This work

4.4. Specificity

Specificity for the modified electrode (BSA/ab/EDC-NHS/AuNP/LIG) was conducted through a cross-reactivity in a PBS solution containing testosterone, cortisone, and 17-hydroxyprogesterone (17-OHP) shown in **Figure 4.9.** They are known to have similar structures to cortisol, making them prime candidates for evaluating the binding specificity of the biosensor [65-67]. EIS measurements were obtained prior to the 100 nM injection of the interfactant, and 30 minutes after the injection. The percent change in Z_{mod} of each interfactant (n=3) was compared to the response after a 100 nM injection of cortisol. The sensor exhibited a 2.58% response to cortisone, 1.93% to testosterone, 2.40% response to 17-OHP, and a 7.83% response to cortisol. Showing that the sensor exhibited a larger response to cortisol compared to the tested interfactants. The non-specific adsorption of non-target hormones were still detectable. However, it is significantly lower than the sensors response to cortisol, revealing the modified LIG's affinity for cortisol.

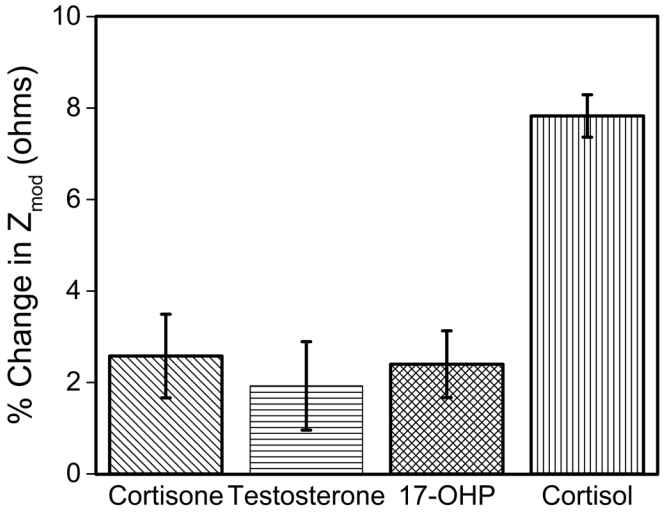

Figure 4.9. Specificity of the fully modified LIG against similarly structured hormones (n=3).

4.5. Cortisol detection in synthetic sweat

Various interferent molecules are found in human sweat, which may impact the electrochemical response. To examine the effect of sweat-based interferents, cortisol dose response from 0.1 pM to 100 nM was performed in a synthetic sweat solution containing commonly found sweat based interferents; 84 μM creatinine, 10 μM ascorbic acid, 0.17 mM glucose, and 59 μM uric acid [68]. Results from the study in **Figure 4.10.** show the sensors performance in synthetic sweat. As with the calibration curve in PBS (**Figure 4.8.(c)),** the sensor exhibited a linear fit (log(Concentration)) over the entirety of the tested range (R^2=0.97) with a LOD of 0.0108 nM. The increase in the LOD when compared to detection in PBS, can be attributed the inherent variability during production effecting results. Thus, the interfactants in the sweat produced no significant effect on the overall performance of the sensor. Indicating it has the potential for use in real human samples.

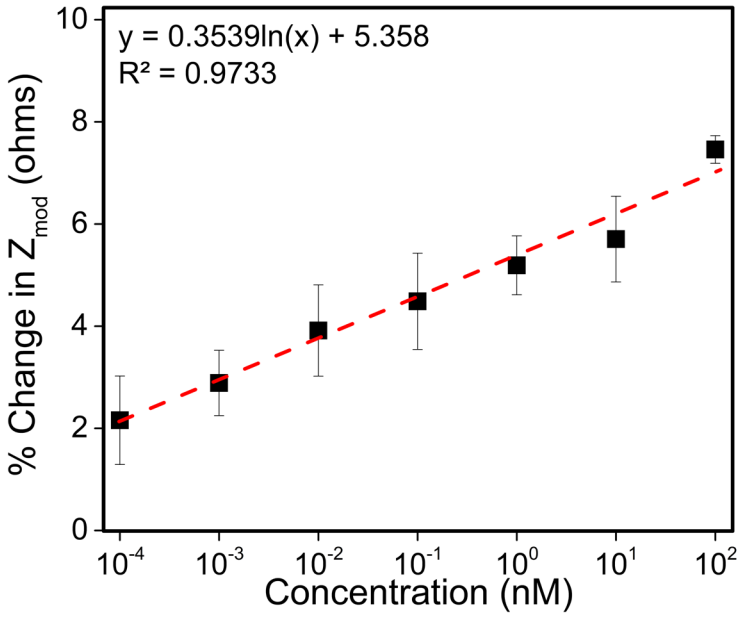

Figure 4.10. Cortisol detection in synthetic sweat (n=3).

4.6. Reproducibility

Reproducibility tests are an excellent way to determine the feasibility of a sensor in real world applications. A large variation in sensor performance makes calibration nearly impossible, thus rendering it useless. To examine the efficacy of the modified electrode, reproducibility was performed by independently incubating five BSA/Ab/AuNP/LIG in 100 nM of cortisol for 30 minutes and comparing the percent change in Z_{mod} (**Figure 4.11.**). The low RSD of 5.93% shows no significant deviation in sensor response and demonstrates its potential for real world applications.

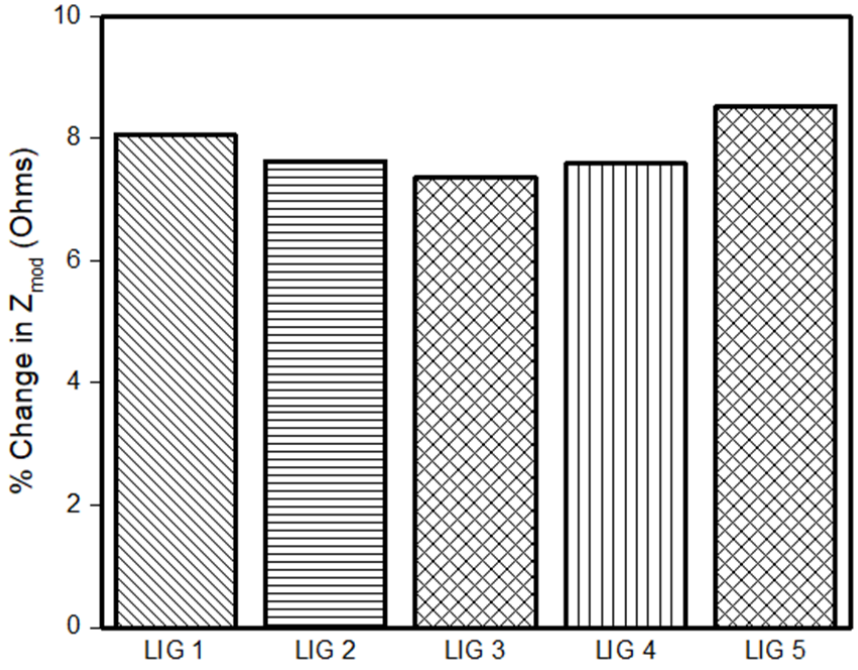

Figure 4.11. Reproducibility performed by comparing percent change in Z_{mod} after 100 nM injection of cortisol for five modified LIG.

4.7. Repeatability

Under the experimental conditions for cortisol dose response, the repeatability of the BSA/ab/AuNP/LIG electrode was investigated by three replicant measurements to obtain Z_{mod} at 200 Hz for each concentration (0.1 pM-100 nM). The corresponding %RSD values in **Table 4.3.** display the biosensors excellent repeatability. A maximum of only 0.41 %RSD observed at 1pM, representing an outstanding analytical performance when compared to recent works [40, 47].

Concentration	%RSD
0.1 pM	0.17
1 pM	0.41
10 pM	0.25
100 pM	0.19
1 nM	0.13
10 nM	0.19
100 nM	0.02

Table 4.3. Repeatability (n=3) for Z_{mod} values obtained at 200 Hz.

5. Conclusions

- A power dose assay was conducted, and the optimized laser parameters obtained were utilized for subsequent production.
- SEM-EDX imaging showed the porous 3D structure of graphene and verified the presence of AuNPs both visually and compositionally.
- XRD analysis of LIG exhibited a short peak at ~26° showing a high degree of graphitization is indicative of a highly graphitized surface. Analysis of the AuNP/LIG peaks of Au face-centered cubic crystallographic structure (38°, 44°, 64°, and 77°), further proving the presence of AuNPs.
- FT-IR indicated successful surface modification at each stage by examining the peaks at wavelengths associated with each chemical bond.
- Raman spectroscopy results showed an intensity ratio, I_D/I_G, 0.475 and 0.548 for LIG and AuNP/LIG.
- Faradaic EIS was performed at each step of surface modification. Found AuNPs decreased the electron transfer resistance (R_{ct}) of the LIG, while each subsequent step in modification (EDC/NHS, ab, BSA) increased the R_{ct}, indicating each step was successful.
- The sensor exhibited a linear fit (log(Concentration)) over the entirety of the tested cortisol range with a high goodness of fit (R^2=0.97) and a LOD (3σ/S) of 0.0085 nM.
- Detection in synthetic sweat should the interfactants in the sweat produced no significant effect on the overall performance of the sensor.

- Specificity experiments showed the sensor exhibited a much larger response to cortisol compared to the tested interfactants, showing the modified LIG's affinity for cortisol.
- Reproducibility and repeatability measurements resulted in a %RSD of 5.93 and 0.41, respectively.

6. Future work

Future work should focus on the full incorporation of the fabricated sensor into a wearable platform with a better sampling, which includes a hydrogel touch pad inside of a PDMS spacer. This platform can be a miniaturized detection platform. To make it a fully POC device in real time, the incorporation of an onboard Bluetooth transceiver wirelessly communicated with a custom-developed smartphone application would be necessary.

6.1. Methodology

The cortisol biosensor incorporated with the hydrogel touch pad was fabricated by the same fabrication and surface chemistry protocols followed above with a few exceptions. Sylgard-184 silicone elastomer (Dow Corning) and its curing agent were mixed in 10:1 (w/w) ratio and cured for 24 h at 65 °C in a large weighing dish and then transferred into a petri dish to form a uniform PDMS sheet (0.5 mm thick), which encases the hydrogel. A vacuum was pulled for 30 minutes to remove air bubbles and if any air bubbles remained a heat gun was used. Once cured, a die set was used to create a single hole was punched at 10 mm in diameter with a 5 mm diameter inner area for the hydrogel. To attach the PDMS spacer to the IDE, both the PDMS spacer and IDE were first treated with oxygen plasma to increase adhesion. A light coating of 5-minute epoxy was applied to the spacer and then carefully placed on to the IDE. Lastly, a balance weight was applied on top to achieve firm adhesion between the PDMS spacer and IDE until the epoxy cured. To add rigidity, a polycarbonate backplate was attached to the IDE using double sided tape.

Figure 6.1. Picture of the IDE touch pad design with a polycarbonate backplate and a PDMS spacer.

The hydrogels were made using a 2% (w/w) agarose gel in water, and then was carefully poured into the spacer to form a uniform hydrogel touch pad.

6.2. Demonstration

To demonstrate the efficacy of the cortisol sensor incorporated with a hydrogel touch pad, a dose response would be performed over the same concentration range of 0.1 pM to 100 nM. New stock solutions would be prepared to account for the decrease in volume. 2 µL of each concentration would be injected on the hydrogel and allowed to defuse through for 30 minutes before running EIS. Results would be expected to be similar to the cortisol dose response previously conducted. However, due to the rate of diffusion and other variables, it would have higher deviations when compared to detection without the touchpad design [88, 89].

Additionally, real sweat analysis would be completed. Sweat collection would be performed by directly placing the index finger on the hydrogel pad for approximately 30

seconds, and then allowed to diffuse through the hydrogel [89]. Single frequency EIS at 200 Hz would be run continuously, starting before contact with the hydrogel and ending 30 minutes after contact to allow time for diffusion. Results would be expected to show a slow and steady decrease in impedance until diffusion of the sweat is complete.

References

1. de Kloet, E.R., M. Joëls, and F. Holsboer, *Stress and the brain: from adaptation to disease.* Nat Rev Neurosci, 2005. **6**(6): p. 463-75.
2. Heinrichs, M., et al., *Social support and oxytocin interact to suppress cortisol and subjective responses to psychosocial stress.* Biol Psychiatry, 2003. **54**(12): p. 1389-98.
3. Bandodkar, A.J., et al., *Wearable Sensors for Biochemical Sweat Analysis.* Annual Review of Analytical Chemistry, 2019. **12**(1): p. 1-22.
4. Russell, E., et al., *The detection of cortisol in human sweat: implications for measurement of cortisol in hair.* Ther Drug Monit, 2014. **36**(1): p. 30-4.
5. Torrente-Rodríguez, R.M., et al., *Investigation of Cortisol Dynamics in Human Sweat Using a Graphene-Based Wireless mHealth System.* Matter, 2020. **2**(4): p. 921-937.
6. Hayes, L.D., et al., *Critical difference applied to exercise-induced salivary testosterone and cortisol using enzyme-linked immunosorbent assay (ELISA): distinguishing biological from statistical change.* Journal of Physiology and Biochemistry, 2014. **70**(4): p. 991-996.
7. Zheng, R., et al., *Development of a highly specific amine-terminated aptamer functionalized surface plasmon resonance biosensor for blood protein detection.* Biomedical Optics Express, 2011. **2**(9): p. 2731-2740.
8. O'Sullivan, C.K. and G.G. Guilbault, *Commercial quartz crystal microbalances – theory and applications.* Biosensors and Bioelectronics, 1999. **14**(8): p. 663-670.
9. Geim, A.K. and K.S. Novoselov, *The rise of graphene.* Nature Materials, 2007. **6**(3): p. 183-191.
10. Justino, C.I.L., et al., *Graphene based sensors and biosensors.* TrAC Trends in Analytical Chemistry, 2017. **91**: p. 53-66.
11. Pumera, M., et al., *Graphene for electrochemical sensing and biosensing.* TrAC Trends in Analytical Chemistry, 2010. **29**(9): p. 954-965.
12. Gao, J., S. He, and A. Nag, *Electrochemical Detection of Glucose Molecules Using Laser-Induced Graphene Sensors: A Review.* 2021. **21**(8): p. 2818.
13. Ye, R., D.K. James, and J.M. Tour, *Laser-Induced Graphene: From Discovery to Translation.* 2019. **31**(1): p. 1803621.
14. Huang, L., et al., *Laser-Induced Graphene: En Route to Smart Sensing.* Nano-Micro Letters, 2020. **12**(1): p. 157.
15. Avinash, K. and F. Patolsky, *Laser-induced graphene structures: From synthesis and applications to future prospects.* Materials Today, 2023. **70**: p. 104-136.

16. Vivaldi, F.M., et al., *Three-Dimensional (3D) Laser-Induced Graphene: Structure, Properties, and Application to Chemical Sensing.* ACS Applied Materials & Interfaces, 2021. **13**(26): p. 30245-30260.

17. Park, B.-W., D.-Y. Yoon, and D.-S. Kim, *Recent progress in bio-sensing techniques with encapsulated enzymes.* Biosensors and Bioelectronics, 2010. **26**(1): p. 1-10.

18. Wang, J., *Electrochemical biosensors: Towards point-of-care cancer diagnostics.* Biosensors and Bioelectronics, 2006. **21**(10): p. 1887-1892.

19. Wu, Q., et al., *Review of Electrochemical DNA Biosensors for Detecting Food Borne Pathogens.* 2019. **19**(22): p. 4916.

20. Ronkainen, N.J., H.B. Halsall, and W.R. Heineman, *Electrochemical biosensors.* Chemical Society Reviews, 2010. **39**(5): p. 1747-1763.

21. Wu, H., et al., *A Comparative Study of Activated Carbons from Liquid to Solid Polymer Electrolytes for Electrochemical Capacitors.* Journal of The Electrochemical Society, 2019. **166**: p. A821-A828.

22. Rajapaksha, R.D.A.A., et al., *Sensitive pH detection on gold interdigitated electrodes as an electrochemical sensor.* Microsystem Technologies, 2018. **24**(4): p. 1965-1974.

23. Dizon, A. and M.E. Orazem, *On the impedance response of interdigitated electrodes.* Electrochimica Acta, 2019. **327**: p. 135000.

24. Mathur, A., et al., *Effect of gap size of gold interdigitated electrodes on the electrochemical immunosensing of cardiac troponin-I for point-of-care applications.* Sensors and Actuators Reports, 2022. **4**: p. 100114.

25. Bratov, A., S. Brosel-Oliu, and N. Abramova, *Label-Free Impedimetric Biosensing Using 3D Interdigitated Electrodes*, in *Label-Free Biosensing: Advanced Materials, Devices and Applications*, M.J. Schöning and A. Poghossian, Editors. 2018, Springer International Publishing: Cham. p. 179-198.

26. Bratov, A., et al., *Three-dimensional interdigitated electrode array as a transducer for label-free biosensors.* Biosensors and Bioelectronics, 2008. **24**(4): p. 729-735.

27. Magar, H.S., R.Y.A. Hassan, and A. Mulchandani, *Electrochemical Impedance Spectroscopy (EIS): Principles, Construction, and Biosensing Applications.* Sensors (Basel), 2021. **21**(19).

28. Harris, A., et al., *Correlation of Impedance and Effective Electrode Area of Doped PEDOT Modified Electrodes for Brain-Machine Interfaces.* Analyst, 2015. **140**.

29. Van Emon, J.M., *1.49 - Immunoassays in Biotechnology*, in *Comprehensive Biotechnology (Second Edition)*, M. Moo-Young, Editor. 2011, Academic Press: Burlington. p. 659-667.

30. Prodromidis, M.I., *Impedimetric immunosensors—A review.* Electrochimica Acta, 2010. **55**(14): p. 4227-4233.

31. Reich, P., et al., *Impedimetric Aptamer-Based Biosensors: Principles and Techniques*, in *Aptamers in Biotechnology*, K. Urmann and J.-G. Walter, Editors. 2020, Springer International Publishing: Cham. p. 17-41.

32. Jagannath, B., S. Muthukumar, and S. Prasad, *Electrical double layer modulation of hybrid room temperature ionic liquid/aqueous buffer interface for enhanced sweat based biosensing.* Analytica Chimica Acta, 2018. **1016**: p. 29-39.

33. Chen, B., et al., *A non-faradaic impedimetric biosensor for monitoring of caspase 9 in mammalian cell culture.* Bioelectrochemistry, 2023. **153**: p. 108456.

34. Jing, M., et al., *Chapter 9 - Nanomaterials for electrochemical energy storage*, in *Frontiers of Nanoscience*, A.J. Wain and E.J.F. Dickinson, Editors. 2021, Elsevier. p. 421-484.

35. Kanagavalli, P., et al., *In-situ redox-active hybrid graphene platform for label-free electrochemical biosensor: Insights from electrodeposition and electroless deposition.* TrAC Trends in Analytical Chemistry, 2021. **143**: p. 116413.

36. Pingarrón, J.M., P. Yáñez-Sedeño, and A. González-Cortés, *Gold nanoparticle-based electrochemical biosensors.* Electrochimica Acta, 2008. **53**(19): p. 5848-5866.

37. Jazayeri, M.H., et al., *Various methods of gold nanoparticles (GNPs) conjugation to antibodies.* Sensing and Bio-Sensing Research, 2016. **9**: p. 17-22.

38. Kumar, S., J. Aaron, and K. Sokolov, *Directional conjugation of antibodies to nanoparticles for synthesis of multiplexed optical contrast agents with both delivery and targeting moieties.* Nature Protocols, 2008. **3**(2): p. 314-320.

39. Li, Y., H.J. Schluesener, and S. Xu, *Gold nanoparticle-based biosensors.* Gold Bulletin, 2010. **43**(1): p. 29-41.

40. Kinnamon, D., et al., *Portable biosensor for monitoring cortisol in low-volume perspired human sweat.* Scientific Reports, 2017. **7**(1): p. 13312.

41. Lee, H.-B., et al., *A wearable lab-on-a-patch platform with stretchable nanostructured biosensor for non-invasive immunodetection of biomarker in sweat.* Biosensors and Bioelectronics, 2020. **156**: p. 112133.

42. Nah, J.S., et al., *A wearable microfluidics-integrated impedimetric immunosensor based on Ti3C2Tx MXene incorporated laser-burned graphene for noninvasive sweat cortisol detection.* Sensors and Actuators B: Chemical, 2021. **329**: p. 129206.

43. Fiore, L., et al., *Microfluidic paper-based wearable electrochemical biosensor for reliable cortisol detection in sweat.* Sensors and Actuators B: Chemical, 2023. **379**: p. 133258.

44. Laochai, T., et al., *Non-invasive electrochemical immunosensor for sweat cortisol based on L-cys/AuNPs/ MXene modified thread electrode.* Biosensors and Bioelectronics, 2022. **203**: p. 114039.

45. Karuppaiah, G., et al., *Towards the development of reagent-free and reusable electrochemical aptamer-based cortisol sensor.* Bioelectrochemistry, 2022. **145**: p. 108098.

46. Tian, G., et al., *Oriented Antibody-Assembled Metal–Organic Frameworks for Persistent Wearable Sweat Cortisol Detection.* Analytical Chemistry, 2023. **95**(35): p. 13250-13257.

47. Kim, K.S., et al., *Highly sensitive and selective electrochemical cortisol sensor using bifunctional protein interlayer-modified graphene electrodes.* Sensors and Actuators B: Chemical, 2017. **242**: p. 1121-1128.

48. Mugo, S.M. and J. Alberkant, *Flexible molecularly imprinted electrochemical sensor for cortisol monitoring in sweat.* Analytical and Bioanalytical Chemistry, 2020. **412**(8): p. 1825-1833.

49. Wanjari, V.P., et al., *Laser-induced graphene-based electrochemical biosensors for environmental applications: a perspective.* 2023. **30**(15): p. 42643-42657.

50. Wan, Z., et al., *Laser induced graphene for biosensors.* 2020. **25**: p. e00205.

51. Liu, J., et al., *Laser-induced graphene (LIG)-driven medical sensors for health monitoring and diseases diagnosis.* 2022. **189**: p. 1-14.

52. You, Z., et al., *Laser-induced noble metal nanoparticle-graphene composites enabled flexible biosensor for pathogen detection.* Biosensors and Bioelectronics, 2020. **150**: p. 111896.

53. Guo, J., et al., *A laser-induced graphene-based electrochemical immunosensor for nucleic acid methylation detection.* Analyst, 2023. **149**(1): p. 137-147.

54. Oliveira, M.E., et al., *Electrochemical Biosensor Based on Laser-Induced Graphene for COVID-19 Diagnosing: Rapid and Low-Cost Detection of SARS-CoV-2 Biomarker Antibodies.* 2022. **5**(1): p. 187-201.

55. Luo, Y., et al., *Fabricating process-electrochemical property correlation of laser-scribed graphene and smartphone-based electrochemical platform for portable and sensitive biosensing.* Biosensors and Bioelectronics, 2023. **237**: p. 115525.

56. Tan, P.S., et al., *Laser Scribing Fabrication of Graphitic Carbon Biosensors for Label-Free Detection of Interleukin-6.* 2021. **11**(8): p. 2110.

57. Yen, Y.-K., G.-W. Huang, and R. Shanmugam, *Laser-scribing graphene-based electrochemical biosensing devices for simultaneous detection of multiple cancer biomarkers.* Talanta, 2024. **266**: p. 125096.

58. Cheng, C., et al., *Bisphenol A Sensors on Polyimide Fabricated by Laser Direct Writing for Onsite River Water Monitoring at Attomolar Concentration.* ACS Applied Materials & Interfaces, 2016. **8**(28): p. 17784-17792.

59. Park, B.-W., et al., *A novel glucose biosensor using bi-enzyme incorporated with peptide nanotubes.* Biosensors and Bioelectronics, 2012. **38**(1): p. 295-301.

60. Park, B.-W., D.-S. Kim, and D.-Y. Yoon, *Surface modification of gold electrode with gold nanoparticles and mixed self-assembled monolayers for enzyme biosensors.* Korean Journal of Chemical Engineering, 2011. **28**(1): p. 64-70.

61. Eissa, S. and M. Zourob, *Competitive voltammetric morphine immunosensor using a gold nanoparticle decorated graphene electrode.* Microchimica Acta, 2017. **184**(7): p. 2281-2289.

62. Park, B.-W., D.-Y. Yoon, and D.-S. Kim, *Formation and modification of a binary self-assembled monolayer on a nano-structured gold electrode and its structural characterization by electrochemical impedance spectroscopy.* Journal of Electroanalytical Chemistry, 2011. **661**(2): p. 329-335.

63. Chulkin, P. and P. Data, *Electrochemical Impedance Spectroscopy as a Tool for Electrochemical Rate Constant Estimation.* J Vis Exp, 2018(140).

64. Hong, B., et al., *Integration of Faradaic electrochemical impedance spectroscopy into a scalable surface plasmon biosensor for in tandem detection.* Opt Express, 2015. **23**(23): p. 30237-49.

65. Arya, S.K., et al., *Antibody functionalized interdigitated μ-electrode (IDμE) based impedimetric cortisol biosensor.* Analyst, 2010. **135**(8): p. 1941-1946.

66. Sekar, M., et al., *Carbon fiber based electrochemical sensor for sweat cortisol measurement.* Scientific Reports, 2019. **9**(1): p. 403.

67. Parlak, O., et al., *Molecularly selective nanoporous membrane-based wearable organic electrochemical device for noninvasive cortisol sensing.* Science Advances. **4**(7): p. eaar2904.

68. Jia, W., et al., *Electrochemical Tattoo Biosensors for Real-Time Noninvasive Lactate Monitoring in Human Perspiration.* Analytical Chemistry, 2013. **85**(14): p. 6553-6560.

69. Saleem, H., M. Haneef, and H.Y. Abbasi, *Synthesis route of reduced graphene oxide via thermal reduction of chemically exfoliated graphene oxide.* Materials Chemistry and Physics, 2018. **204**: p. 1-7.

70. Sneha, K., et al., *Yucca-derived synthesis of gold nanomaterial and their catalytic potential.* Nanoscale research letters, 2014. **9**: p. 627.

71. Li, Y., et al. *Intrinsic Catalytic Activity of Gold/Multi-Walled Carbon Nanotubes Composites in Squaric Acid-Iron(II/III) System*. Catalysts, 2018. **8**, DOI: 10.3390/catal8050187.

72. Wright, M.C., V.L. Long, and S.J. McDanels, *Chapter 3 - The evolution of failure analysis at NASA's Kennedy Space Center and lessons learned*, in *Handbook of Materials Failure Analysis with Case Studies from the Aerospace and Automotive Industries*, A.S.H. Makhlouf and M. Aliofkhazraei, Editors. 2016, Butterworth-Heinemann: Boston. p. 57-73.

73. Lamberti, A., et al., *New insights on laser-induced graphene electrodes for flexible supercapacitors: tunable morphology and physical properties.* Nanotechnology, 2017. **28**(17): p. 174002.

74. Crous, A. and H. Abrahamse, *Effective Gold Nanoparticle-Antibody-Mediated Drug Delivery for Photodynamic Therapy of Lung Cancer Stem Cells.* Int J Mol Sci, 2020. **21**(11).

75. Barnawi, N., S. Allehyani, and R. Seoudi, *Biosynthesis and characterization of gold nanoparticles and its application in eliminating nickel from water.* Journal of Materials Research and Technology, 2022. **17**: p. 537-545.

76. Zhu, G., et al., *β-Cyclodextrin non-covalently functionalized single-walled carbon nanotubes bridged by 3,4,9,10-perylene tetracarboxylic acid for ultrasensitive electrochemical sensing of 9-anthracenecarboxylic acid.* Nanoscale, 2012. **4**(18): p. 5703-5709.

77. Ozhukil Kollath, V., et al., *Systematic Processing of β-Tricalcium Phosphate for Efficient Protein Loading and In Vitro Analysis of Antigen Uptake.* 2013. **15**(4): p. 295-301.

78. Gole, A. and C.J. Murphy, *Seed-Mediated Synthesis of Gold Nanorods: Role of the Size and Nature of the Seed.* Chemistry of Materials, 2004. **16**(19): p. 3633-3640.

79. Alhazmi, H.A. *FT-IR Spectroscopy for the Identification of Binding Sites and Measurements of the Binding Interactions of Important Metal Ions with Bovine Serum Albumin*. Scientia Pharmaceutica, 2019. **87**, DOI: 10.3390/scipharm87010005.

80. Guo, C., et al., *Spectroscopic study of conformation changes of bovine serum albumin in aqueous environment.* Chinese Chemical Letters, 2019. **30**(6): p. 1302-1306.

81. Shams, N., et al., *Electrochemical sensor based on gold nanoparticles/ethylenediamine-reduced graphene oxide for trace determination of fenitrothion in water.* RSC Advances, 2016. **6**: p. 89430-89439.

82. Xiong, K., et al., *Enhanced bovine serum albumin absorption on the N-hydroxysuccinimide activated graphene oxide and its corresponding cell affinity.* Materials Science and Engineering: C, 2017. **81**: p. 386-392.

83. Kurra, N., et al., *Laser-derived graphene: A three-dimensional printed graphene electrode and its emerging applications.* Nano Today, 2019. **24**: p. 81-102.

84. Yang, X., et al., *Graphene uniformly decorated with gold nanodots: in situ synthesis, enhanced dispersibility and applications.* Journal of Materials Chemistry, 2011. **21**(22): p. 8096-8103.

85. Shoute, L.C.T., et al., *Label-free impedimetric immunosensor for point-of-care detection of COVID-19 antibodies.* Microsystems & Nanoengineering, 2023. **9**(1): p. 3.

86. Mark, E., et al., *The Apparent Constant-Phase-Element Behavior of an Ideally Polarized Blocking Electrode.* Journal of the Electrochemical Society, 2007. **154**: p. C81.

87. Radha Shanmugam, N., et al., *Ultrasensitive nanostructure sensor arrays on flexible substrates for multiplexed and simultaneous electrochemical detection of a panel of cardiac biomarkers.* Biosensors and Bioelectronics, 2017. **89**: p. 764-772.

88. Nagamine, K., et al., *Noninvasive Sweat-Lactate Biosensor Emplsoying a Hydrogel-Based Touch Pad.* Scientific Reports, 2019. **9**(1): p. 10102.

89. Kim, G.J. and K.O. Kim, *Novel glucose-responsive of the transparent nanofiber hydrogel patches as a wearable biosensor via electrospinning.* Scientific Reports, 2020. **10**(1): p. 18858.